Journal of Nuclear Materials 557 (2021) 153303

Contents lists available at ScienceDirect

Journal of Nuclear Materials

journal homepage: www.elsevier.com/locate/jnucmat

Investigation of δ zirconium hydride morphology in a single crystal using quantitative phase field simulations supported by experiments

P.-C.A. Simon[a,d,*], Larry K. Aagesen[d], Andrea M. Jokisaari[d], Long-Qing Chen[b], Mark R. Daymond[e], Arthur T. Motta[a], Michael R. Tonks[c]

[a] Ken and Mary Alice Lindquist Department of Nuclear Engineering, The Pennsylvania State University, University Park, PA, 16802, USA
[b] Department of Materials Science and Engineering, The Pennsylvania State University, University Park, PA, 16802, USA
[c] Department of Materials Science and Engineering, University of Florida, Gainesville, FL, 32611, USA
[d] Computational Mechanics and Materials Department, Idaho National Laboratory, Idaho Falls, ID, 83415, USA
[e] Department of Mechanical and Materials Engineering, Queen's University, Kingston, Ontario, K7L 2N8, Canada

ARTICLE INFO

Article history:
Received 10 April 2021
Revised 26 August 2021
Accepted 15 September 2021
Available online 16 September 2021

Keywords:
Microstructure evolution
Zirconium hydrides
Phase field modeling
Experimental comparison
Nuclear materials

ABSTRACT

In light water nuclear reactors, waterside corrosion of the cladding material leads to the production of hydrogen, a fraction of which is picked up by the zirconium cladding and precipitates into brittle hydride particles. These nanoscale hydride particles aggregate into mesoscale hydride clusters. The principal stacking direction of the nanoscale hydrides precipitated in the cladding tube changes from circumferential in the absence of applied stress to radial under circumferential applied stress. A quantitative phase field model has been developed to predict the hydride morphology observed experimentally and identify the mechanisms responsible for nanoscale hydride stacking. The model focuses on nanoscale hydride precipitation in a single zirconium grain with a detailed description of the anisotropic elastic contribution. The model predictions concerning the shape, orientation, and stacking behavior of nanoscale hydride are analyzed and compared with experimental observations. The model accurately accounts for the experimentally observed elongated nanoscale hydride shape and the stacking of hydrides along the basal plane of the hexagonal zirconium matrix. When investigating the role of applied stress in hydride morphology, the model challenges some of the mechanisms previously proposed to explain hydride reorientation. Although hydride reorientation has been hypothesized to be caused by a change in nanoscale hydride shape, the current study shows that these mechanisms are unlikely to occur.

Published by Elsevier B.V.

1. Introduction

1.1. Zirconium hydride morphology

Zirconium alloys offer good high temperature corrosion resistance in water, low thermal neutron absorption cross-section, good thermal conductivity, and adequate mechanical properties. These properties make them appropriate as cladding materials for Light Water Reactors [1,2]. However, zirconium cladding can be prone to hydrogen embrittlement due to the formation of brittle hydrides. As the cladding corrodes, hydrogen is created as a byproduct, and a fraction of the hydrogen produced is picked up by the cladding [3–5]. While corrosion is the primary source of hydrogen, hydrogen produced by radiolysis of the surrounding water due to irradiation and the hydrogen present in the materials of the reactor can also be picked up by the cladding. Once the hydrogen concentration reaches the solubility limit in the material, it precipitates into brittle hydride particles [6–9]. Different hydride phases may precipitate, depending on the conditions [2,10,11]. At normal reactor operating conditions, the precipitation of δ-hydrides is favored over other hydride phases, especially for slower cooling rates [11–14]. Because hydrides are commonly observed as δ-$ZrH_{1.66}$ in nuclear fuel cladding [2], the current work focuses on δ-hydride morphology.

Hydride particles form a multi-scale structure, in which nanoscale hydrides of a few dozens of nanometers aggregate to form long mesoscale hydrides [2,15,16]. Observed at low magnification, mesoscale δ-hydrides appear as platelets, whose length, density, and orientation depend on several factors, including substrate texture, grain boundary density and orientation, cooling rate during precipitation, external stress, and thermomechanical treatment [2,17–19]. In particular, whereas mesoscale hydrides tend to orient circumferentially in a zirconium cladding tube, the presence

* Corresponding author.
E-mail address: pierreclement.simon@inl.gov (P.-C.A. Simon).

https://doi.org/10.1016/j.jnucmat.2021.153303
0022-3115/Published by Elsevier B.V.

of an external tensile stress applied in the circumferential direction during cooling can lead to mesoscale hydride structures with an overall radial orientation. The change from circumferential to radial hydrides is called hydride reorientation and has been extensively studied because of its importance in crack propagation [2,20–29]. Because hydrides are brittle, hydride reorientation can ease crack propagation through the cladding thickness, which may result in the release of fission products. Understanding mesoscale hydride morphology is thus crucial to assess cladding integrity. Previous experimental studies have quantified the stress needed to observe hydride reorientation (the threshold stress), and reported values vary between 50 and 220 MPa [2,29–34]. Several factors can influence hydride morphology and the threshold stress, including stress state, hydrogen content, texture, grain size, cold work, and cooling rate during precipitation, which can account for the disparity in the reported measurements.

The hydride structures observed at the mesoscale are believed to be the result of mechanisms happening at lower length scales [2]. Unfortunately, mesoscale hydrides are often thought of as single hydride particles with a different orientation relationship with the matrix depending on applied stress, rather than a stacking of nanoscale hydrides. This confusion has hindered the understanding of the formation of long mesoscale hydrides and of the reorientation process. High magnification micrographs reveal that the long mesoscale hydrides are, in fact, aggregates of nanoscale hydrides disks stacked either circumferentially or radially [2,15,35,36] across many grains. Moreover, Transmission Electron Microscopy (TEM) and Electron Backscatter Diffraction (EBSD) studies show the multi-scale structure of the hydrides at high magnification and determine their orientation relationship with the matrix of individual grains. Independent of their stacking direction, the orientation relationship between the α-Zr matrix and the δ-$ZrH_{1.66}$ precipitates has been observed to be $\{0001\}_\alpha \| \{111\}_\delta$; $< 11\bar{2}0 >_\alpha \| < 1\bar{1}0 >_\delta$ [2,16,37–43], with some studies reporting a low frequency of $\{10\bar{1}7\}_\alpha \| \{111\}_\delta$ [35,41]. This suggests that hydride reorientation might be caused by different hydride particle stacking to accommodate the external stress rather than resulting from a change in the habit planes of the precipitates.

1.2. Previous work on zirconium hydride morphology modeling

Hydride precipitation into specific microstructures with or without applied stress is a complex phenomenon that has been extensively studied experimentally. Modeling efforts have been produced to complement experimental work and understand the underlying mechanisms governing hydride morphology. At the mesoscale, phase field modeling has emerged as a powerful and adaptable method to study microstructure evolution in materials [44–47]. As such, phase field modeling is relevant for the study of complex multi-physics systems like zirconium hydrides [2,48–55].

Several models have been proposed to account for hydride morphology, both without and with applied stress. Some assume that mesoscale hydrides can be described as single platelets that would grow along the basal plane without applied stress, and perpendicular to the basal plane under applied stress. In Refs. [50,51,56], the authors showed that the anisotropy of the strain due to volume misfit between the two phases is responsible for the elongated shape of the hydrides along the circumferential direction. Then, they assumed that if a sufficient tensile stress is applied in the circumferential direction, this anisotropy could be reduced or inverted so that hydride platelets would grow radially rather than circumferentially to accommodate the stress. Unfortunately, the anisotropy of the volume misfit is rather large and the stress required by this mechanism to lead to reorientation is between 1.5 and 2.5 GPa [50,51,56]. Even when the potential effect of the successive phase transformations of other hydride phases into δ-hydrides is taken into account [50], the threshold stress calculated by the phase field model remains unreasonably high compared to experimental observations [2,33]. This discrepancy is attributed to the fact that the mesoscale hydride microstructure cannot be accurately modeled without describing the mechanisms governing the stacking of nanoscale hydride into mesoscale hydrides.

More recent phase field models have introduced the nanoscale hydride structure to explain the mesoscale hydride microstructure. This mechanism was investigated in recent studies by Han et al. and Heo et al. [52,53]. In the model proposed by Han et al., the anisotropy of the interfacial free energy is defined so that nanoscale hydrides stack along the $\{10\bar{1}7\}_\alpha$ plane without applied stress to correspond to some of the experimental observations [35,41]. Then, as the magnitude of the applied stress increases, the stacking direction progressively becomes more radial due to a change in nanoscale hydride shape, as shown in Fig. 18 in Ref. [52]. In this model, the magnitude of the applied stress is reasonably close to experimental measurements, which is a significant improvement compared to previous efforts. The approach from Heo et al. is slightly different. Rather than using an anisotropic free energy, they argue that the applied stress results in a loss of coherency at the α-Zr/δ-$ZrH_{1.66}$ interface which reduces the strains in specific directions. As the magnitude of the applied stress increases, the loss of coherency increases, which leads to a change in nanoscale hydride shape and stacking direction, as shown in Fig. 5 in Ref. [53]. In this model, the link between the magnitude of the applied stress and the loss of coherency is not quantitatively defined. It is thus difficult to relate which applied stress would lead to which microstructure for validation purposes.

However, both these recent models involve the presence of a large shear strain in the elastic description of the δ-hydrides. In addition to the strain due to the 17% volume misfit between the two phases [2], these authors introduce a large shear strain of 19% in the model, arguing that it originates from the HCP to FCC phase transformation. We discuss the validity of such a large shear strain further in Section 2.2.3, but such an assumption contradicts the shear mechanism proposed by Zhang et al. [57] and supported by Louchez et al. [58], which offers a formation path for δ-hydrides leading to shear components equal to zero. For that reason, the current study did not introduce a shear strain, which significantly changes the elastic description of the system. Nevertheless, Han et al. and Heo et al. have found the shear strain necessary to explain nanoscale hydride stacking and hydride morphology [52,53].

1.3. Motivation and aims of the current work

As discussed above, despite considerable experimental and modeling efforts to understand hydride morphology and reorientation under applied stress, the mechanisms behind mesoscale hydride morphology are still unknown. This study aims at answering the following question: which physics and mechanisms govern the formation of specific hydride microstructures? This work hypothesizes that the elastic property anisotropy of the α-Zr and δ-$ZrH_{1.66}$ phases is primarily responsible for the nanoscale hydride elongated shape and stacking behavior. To test this hypothesis, a quantitative phase field model of nanoscale hydrides has been developed to predict the hydride morphology observed experimentally and identify which mechanisms are responsible for circumferential and radial hydride precipitation. The current phase field model differs significantly from previous modeling efforts by the description of the elastic properties of the α-Zr and δ-$ZrH_{1.66}$ phases and in the potential mechanisms that are being accounted for to explain hydride morphology. The elastic properties are derived from lower-scale modeling efforts, crystallographic considerations, and experimental measurements and do not include the large shear strain

introduced by previous studies. Moreover, the current study focuses on the effect of elastic interaction between hydride particles to investigate their stacking behavior. The phase field model's predictions are carefully compared with experimental observations to support the mechanisms proposed in this study.

The quantitative phase field model applied to the α-Zr/δ-$ZrH_{1.66}$ system is described in Section 2, where the elastic contribution is carefully detailed. The phase field model is then used to investigate hydride morphology in a single zirconium grain under different precipitation conditions in Section 3. In Section 3.1, we focus on the morphology of a single hydride as predicted by the phase field model in the absence of applied stress. The effect of applied stress on an isolated nanoscale hydride particle is investigated in Section 3.2. Because mesoscale hydride morphology depends on the stacking behavior of nanoscale hydrides, the following sections, i.e. Sections 3.3 and 3.4, present how hydrides interact and stack, without and with external applied stress, respectively. These results are then compared to experimental observations in Section 4 to support the validity of the model and its assumptions. We then discuss the results and their significance regarding the phase field predictions of hydride morphology in Section 5, where potential ideas for future work are also discussed. We conclude the manuscript in Section 6.

2. Phase field modeling of the α-Zr/δ-$ZrH_{1.66}$ system

In the phase field approach, the microstructure is defined by a set of continuous field variables such as the solute concentration that are evolved in time and space based on the reduction of the free energy of the system [44,45]. It allows the coupling of different thermodynamical driving forces for microstructure evolution, making it possible to include the effect of bulk and interfacial energy, elastic energy, plastic deformation, as well as other sources of energy. As such, phase field modeling is relevant for the study of complex multi-physics systems such as zirconium hydrides [2,48–53,55]. Modeling can complement the understanding from experimental studies by isolating individual physical processes and identifying which mechanisms govern hydride morphology, and which ones do not.

The main hypothesis of this work is that the elastic property anisotropy of the α-Zr and δ-$ZrH_{1.66}$ phases is primarily responsible for the nanoscale hydride elongated shape and stacking behavior. Accordingly, the current phase field model attempts to capture most of the possible sources of elastic anisotropy of the system, including in the stiffness tensors or the lattice strains present. The model presented in this work differs from previous models by the description of the elastic contributions included, which is described in Section 2.2.3.

The interfacial chemical energy treatment of the current phase field model is based on the approach developed by Kim, Kim, and Suzuki (KKS) [59]. It decouples the bulk and interfacial free energies by defining the interface as a mixture of different phases. This decoupling allows for the interfacial length to be defined independently from the bulk and interfacial energy, thus resulting in lower computational costs than the approach developed by Wheeler, Boettinger, and McFadden (WBM model) [60]. The grand potential formulation is another approach that defines the interfacial thickness independently of the bulk and interfacial free energies [61–70]. However, the grand potential model requires more restrictive assumptions and makes modeling the impact of lattice strain on hydrogen diffusion challenging [70], which is a critical mechanism in the behavior of hydrogen in zirconium alloys. Because of its lower computational costs and higher versatility, the KKS model was chosen to model the microstructure evolution of the α-Zr/δ-ZrH system.

2.1. General formulation of the phase field model

In our phase field model, the microstructure of the α-Zr/δ-ZrH system is described by a composition variable field c, which represents the total atomic fraction of hydrogen, and order parameter fields η_ν with ν representing a given phase variant ($\nu = \alpha_i, \delta_i$). Each variable field η_ν is a phenomenological phase descriptor that is equal to 1 in its phase, equal to 0 in other phases, and varies continuously from 0 to 1 at the interface. In this study, the α-Zr phase is described by a single order parameter η_α, and the δ-ZrH phase is described by two different order parameters η_{δ_1} and η_{δ_2} to represent the different elastic variants introduced below. In the rest of the manuscript, $\vec{\eta}$ will designate the vector of order parameters $\eta_\alpha, \eta_{\delta_1}$, and η_{δ_2}.

The evolution of the continuous variables of the phase field model is governed by the reduction of the total free energy. In this study, the total free energy is given as

$$\begin{aligned} F_{tot} &= \int_V f_{tot} dV \\ &= \int_V (f_{chem}(c, \vec{\eta}) + f_{int}(\vec{\eta}) + f_{el}(c, \vec{\eta})) dV, \end{aligned} \tag{1}$$

where f_{tot} is the total free energy density, f_{chem} is the chemical free energy density, f_{int} is the contribution from the interface to the total free energy, and f_{el} is the elastic energy density.

In the KKS model formulation [59], the total atomic fraction of hydrogen c is described as an interpolation of the hydrogen atomic fractions in the α and δ phases and variants, respectively c_α and c_{δ_i} $(i = 1, 2)$,

$$c = \sum_\nu h_\nu(\vec{\eta}) c_\nu, \tag{2}$$

where h_ν is an interpolation function for phase ν that varies continuously from $h_\nu(\eta_\nu = 0) = 0$ to $h_\nu(\eta_\nu = 1) = 1$ with $\partial h_\nu / \partial \eta_\nu (\eta_\nu = 0) = 0$ and $\partial h_\nu / \partial \eta_\nu (\eta_\nu = 1) = 0$. Several different interpolation functions exist, but in this study, h_ν are defined as described in [71] as

$$h_\nu = \frac{\eta_\nu^2}{\sum_{\nu'} \eta_{\nu'}^2}. \tag{3}$$

Using the interpolation functions described in [71] ensures that the total weight of the phase free energy contributions is equal to 1 since $\sum_\nu h_\nu = 1$. In addition, the total potential in each phase is defined to be equal to each other at a given location using [59]

$$\mu = \frac{\partial f_{tot}}{\partial c_\alpha} = \frac{\partial f_{tot}}{\partial c_{\delta_i}} \tag{4}$$

to ensure that the interface is defined as a mixture of the two phases with different compositions, but with the same total potential.

The evolution of the continuous variables of the phase field model is governed by the Cahn-Hilliard and the Allen-Cahn equations. Since the model does not include the gradient energy in composition, the Cahn-Hilliard equation [59,72] becomes a diffusion equation

$$\frac{\partial c}{\partial t} = \nabla \cdot M \nabla \left(\frac{\delta F_{tot}}{\delta c} \right), \tag{5}$$

which dictates the evolution of the hydrogen composition. The hydrogen mobility M will be derived in Section 2.3. The Allen-Cahn equation [59,73]

$$\frac{\partial \eta_\nu}{\partial t} = -L \left(\frac{\delta F_{tot}}{\delta \eta_\nu} \right) \tag{6}$$

governs the evolution of the phase descriptors η_ν. The mobility of the interface L is assumed to be equal for all interfaces, and will be defined in Section 2.3.

2.2. Description of the α-Zr/δ-$ZrH_{1.66}$ system

Accurate values of the phase field parameters such as the chemical, elastic, and interfacial energies are crucial for the development of a quantitative phase field model. To the extent possible, in this work, these values are based either on previously published experimental measurements or on atomistic calculations. Although only isothermal simulations are considered in this study, when available, the temperature dependence of some of the parameters of the model is included. This ensures that the proper parameters are being used at the desired temperature of the study, it makes it easier to perform isothermal simulations at different temperatures, and it allows the model to be easily extended to perform simulations with varying temperatures.

2.2.1. Chemical free energy

The chemical free energy density of the system f_{chem} is defined as

$$f_{chem}(c_\nu, \vec{\eta}) = \sum_\nu h_\nu(\vec{\eta}) f^\nu_{chem}(c_\nu), \tag{7}$$

where f^α_{chem} and f^δ_{chem} are the chemical free energy densities of the α and δ phases, respectively [59]. It is important to note that the chemical free energy density f^δ_{chem} is valid for all δ variants, as only the elastic description changes. In this study, the chemical free energy densities are based on CALPHAD Gibbs free energies. CALPHAD-based Gibbs free energies as a function of composition and temperature were determined by Dupin et al. [74] and are reproduced in Appendix A. However, the presence of natural logarithm terms in these formulas can make these expressions numerically challenging to use. As a result, parabolic approximations are used in this work for f^α_{chem} and f^δ_{chem}:

$$f^\nu_{chem}(c_\nu) = \frac{1}{2}\lambda_\nu (c_\nu - c^\nu_\nu)^2 + f^0_\nu, \tag{8}$$

with ν indicating the α or δ phases, λ_ν the free energy coefficient, c_ν the hydrogen atomic fraction in phase ν, c^ν_ν the atomic fraction of the minimum of the parabola, which differs from equilibrium concentration c^{eq}_ν, and f^0_ν the minimum energy value of the parabola for phase ν. For each temperature, these parameters are derived to fit the CALPHAD free energies G_α and G_δ. First, the equilibrium concentrations c^{eq}_α and c^{eq}_δ are obtained using the common tangent method between G_α and G_δ. Then, solving

$$f^\nu_{chem}(c^{eq}_\nu) = G_\nu(c^{eq}_\nu), \tag{9}$$

$$\frac{\partial f^\nu_{chem}}{\partial c}(c^{eq}_\nu) = \frac{\partial G_\nu}{\partial c}(c^{eq}_\nu), \tag{10}$$

and

$$\frac{\partial^2 f^\nu_{chem}}{\partial c^2}(c^{eq}_\nu) = \frac{\partial^2 G_\nu}{\partial c^2}(c^{eq}_\nu) \tag{11}$$

for $\nu = \alpha$ and δ ensures that the parabolic energies and their first and second derivatives are equal to those from the CALPHAD free energies at the equilibrium compositions.

Fig. 1 shows the results of the parabolic approximation of the CALPHAD free energies of the two phases at $T = 550$ K, and Table 1 presents the values of the parameters used in Eq. (8) for the parabolic approximation. It is important to note that the parameters c^ν_ν are not defined equal to the equilibrium concentrations c^{eq}_ν. The use of the parabolic approximation (dashed lines) is justified because they provide the same equilibrium atomic fractions, similar energies, the same common tangent, and the same curvatures as the CALPHAD free energies (solid lines). The departure from the CALPHAD free energies happens further away from the equilibrium compositions, whereas the phase atomic fractions tend to stay near equilibrium in the model. Moreover, the use of parabolic approximations significantly reduces the computational cost of the simulations. Moreover, it is important to note that, as shown in Appendix B, this description of the chemical free energy is directly related to the solubility limit (TSS_D) of the system.

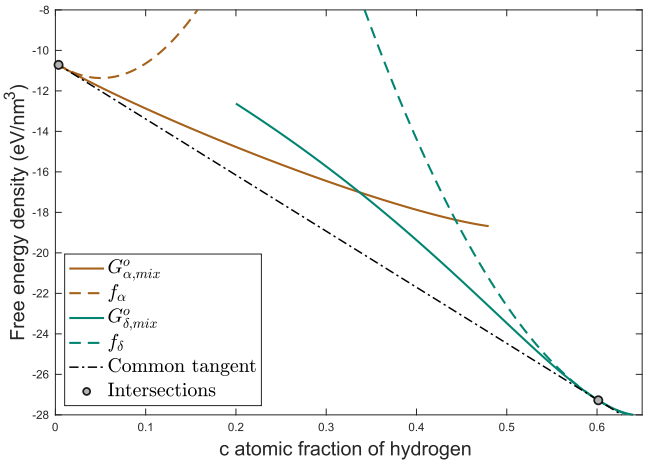

Fig. 1. Parabolic approximations of the CALPHAD free energies of the α-Zr/δ-$ZrH_{1.66}$ ($c \approx 0.62$) system at $T = 550$ K. The common tangent is shown, as well as the intersection points between the CALPHAD free energies, the common tangent, and the parabolic approximations (dashed lines). The CALPHAD free energies and the parabolic approximation share the same common tangent, thus providing the same equilibrium compositions. The departure from the CALPHAD free energies becomes significant only far from the equilibrium concentrations, which is acceptable since the phase atomic fractions tend to stay near equilibrium in the model.

Table 1
Parameters of the parabolic approximation of the chemical free energy densities for the α-Zr/δ-ZrH system at $T = 550$ K.

Parameter	Value	Parameter	Value	Units
λ_α	589.19	λ_δ	361.29	$\frac{eV}{nm^3}$
c^ν_α	587	c^ν_δ	22746	wt.ppm
f^0_α	−11.36	f^0_δ	−28.34	$\frac{eV}{nm^3}$

2.2.2. Interfacial free energy

The interface contribution to the total free energy is given by

$$f_{int}(\vec{\eta}) = wg(\vec{\eta}) + \frac{\kappa}{2}\sum_\nu \|\nabla \eta_\nu\|^2, \tag{12}$$

where κ is a gradient energy coefficient [59], g is a double-well potential defined as

$$g(\vec{\eta}) = \sum_\nu \left(\frac{\eta^4_\nu}{4} - \frac{\eta^2_\nu}{2}\right) + \sum_\nu \left[\sum_{\nu' \neq \nu} \frac{\gamma_{\nu\nu'}}{2}\eta^2_\nu \eta^2_{\nu'}\right] + \frac{1}{4}, \tag{13}$$

where w is the height of this double-well potential, and $\gamma_{\nu\nu'} = 1.5$ [75,76]. The values for κ and w are set by the values of the interfacial width l and the interface energy γ as [59,75,76]

$$\kappa = \frac{3}{4.4}\gamma l \tag{14}$$

and

$$w = 6.6\frac{\gamma}{l}. \tag{15}$$

The energy of the α-Zr/δ-$ZrH_{1.66}$ interface is likely anisotropic. However, because an anisotropic description of the hydride interfacial energy is not yet available, the interfacial energy is assumed to be isotropic, as has been done in previous studies [48,50,77,78]. Notably, assuming that the interfacial energy is isotropic might influence the predicted shape of the hydride particles. Ideally, an

Table 2
Interfacial parameters for the α-Zr/δ-ZrH system.

Parameter	Value	Units	Ref.
γ	1.2483	$\frac{eV}{nm^2}$	[79,80]
l	1	nm	
κ	0.85	$\frac{eV}{nm}$	
w	8.24	$\frac{eV}{nm^3}$	

anisotropic interfacial energy would be provided by lower length scale simulations such as DFT calculations. However, to the authors' knowledge, these are currently unavailable due to the difficulty of accurately simulating the α-Zr/δ-ZrH$_{1.66}$ interfaces. Due to a lack of available data on the interfacial energy, the current study thus focuses on the effect of the anisotropy of elastic properties of the system on hydride shape and stacking behavior. The potential consequences of this assumption are discussed in more detail in Section 5. The value of the interfacial energy was taken from ab-initio calculations shown in Table 2 [79]. The properties of interfaces between hydride variants are also unknown. In this study, for consistency and simplicity, they are assumed to have the same thickness and energy as α-Zr/δ-ZrH$_{1.66}$ interfaces. Following a convergence study, the value of the interfacial thickness is taken equal to $l = 1$ nm to limit computational costs while resolving the microstructure for features on the order of 10 nm. The values derived for κ and w are given in Table 2.

2.2.3. Elastic free energy

This study hypothesizes that the anisotropy of eigenstrains and the stiffness tensors is responsible for the elongated shape of the nanoscale hydrides and hydride stacking. As a result, the elastic contribution is described with particular attention in the current model. In this model, the elastic free energy density f_{el} is derived using the Khachaturyan's strain interpolation scheme (KHS) [81–83] as opposed to the Voight-Taylor's elastic energy interpolation scheme (VTS) [84] or other schemes [70,85–91]. The KHS scheme has been commonly used in phase field models. Some of these elastic schemes introduce an excess interfacial energy at the interface of the phase field model, which can influence predictions. The KHS scheme has been shown to introduce a smaller excess of energy than the VTS model [70,90]. Recent efforts have proposed schemes that introduce no excess elastic energy at the interface [91] and should be considered for future work. The KHS scheme consists of deriving the strain independently in each phase, and then interpolating the strains and stiffness tensors across phases before deriving the stress and the elastic energy. In the KHS model, the stiffness tensor and the eigenstrain are interpolated to result in

$$C_{ijkl} = \sum_{\nu} h_{\nu}(\vec{\eta}) C_{ijkl,\nu}, \tag{16}$$

and

$$\epsilon^{el}_{ij} = \epsilon^{tot}_{ij} - \sum_{\nu} h_{\nu}(\vec{\eta}) \epsilon^{*}_{ij,\nu}, \tag{17}$$

where $C_{ijkl,\alpha}$ and $C_{ijkl,\delta}$ are the stiffness tensors for the α-Zr and δ-ZrH phases, respectively, ϵ^{el}_{ij} is the elastic strain, ϵ^{tot}_{ij} is the total strain, and $\epsilon^{*}_{ij,\alpha}$ and $\epsilon^{*}_{ij,\delta}$ are the eigenstrains that define the lattice strains.

Once the stiffness tensor and the strain are defined, the stress σ_{ij} is derived assuming linear elasticity. As discussed below, assuming linear elasticity simplifies the model but ignores the plastic deformation happening during hydride precipitation [2,11,92–94]. The mechanical equilibrium equation is then solved assuming quasi-static conditions

$$\nabla \cdot \sigma_{ij} = 0. \tag{18}$$

Table 3
Stiffness tensor values at $T_{ref} = 4$ K and linear temperature dependence coefficients from Ref. [95].

	11	12	13	33	44	Units
$C_{ij}^{T_{ref}}$	155.4	67.2	64.6	172.5	36.3	GPa
$\Delta C_{ij}(\times 10^2)$	4.5	1.6	0.11	3.21	1.39	GPa·K^{-1}

The elastic free energy contribution to the system is then derived as

$$f_{el} = \frac{1}{2} C_{ijkl} \epsilon^{el}_{ij} \epsilon^{el}_{kl}. \tag{19}$$

To account for the anisotropy of the elastic contribution, the stiffness tensors and the eigenstrains should accurately describe the crystal structures and properties of the α-Zr and δ-ZrH phases. In the following paragraphs, we describe the stiffness tensors and the eigenstrains of the zirconium and the hydride and how they vary with temperature. We explain how they were derived for the current work, and how it differs from previous models. When available, we use experimental measurements of the desired properties. However, when experimental measurements are not available, we use lower-scale calculations and discuss their validity.

Stiffness tensors: The stiffness tensor of the HCP α-zirconium has been experimentally determined from 4 K to 1155 K using an ultrasonic wave interference technique [95]. The individual components of the stiffness tensor for α-zirconium have been found to vary linearly with temperature, so, using the Voigt notation, the value of the component ij can be described as

$$C_{ij}(T) = C_{ij}^{T_{ref}} + \Delta C_{ij}(T - T_{ref}), \tag{20}$$

where T is the temperature in K, $T_{ref} = 4$ K is the reference temperature, $C_{ij}^{T_{ref}}$ is the stiffness tensor component at the reference temperature, and ΔC_{ij} is the slope with temperature. Due to hexagonal symmetry, the stiffness tensor can be described with only five unique components. If the direction of the subscript 11 of the stiffness tensor corresponds to the $\{11\bar{2}0\}_{\alpha}$ direction, 22 corresponds to the $\{\bar{1}100\}_{\alpha}$ direction, and 33 corresponds to the $\{0001\}_{\alpha}$ direction, then $C_{11} = C_{22}, C_{13} = C_{23}, C_{44} = C_{55}$, and $C_{66} = (C_{11} - C_{12})/2$. Table 3 provides the values for the stiffness tensor coefficients published by Fisher et al. [95], as well as the linear temperature coefficients.

Measuring the stiffness tensor of the hydride phases is extremely challenging and no experimental data is readily available. However, several DFT studies have determined the stiffness tensors of the δ-ZrH$_{1.66}$ phase [96–100]. Each study selected several possible spatial groups for δ-hydrides, and derived their lattice parameters, stiffness tensors, and stability. Unfortunately, most of the stable structures predicted by these studies are not FCC, which contradicts experimental observations [12,14,101–103]. The difference between experimental measurements and DFT predictions can be explained by the fact that these atomistic models cannot take into account the effect of temperature and correspond to $T = 0$ K. The relative structure stability, as well as their tetragonality, are expected to vary as temperature increases, as noted by Zhu et al. [99]. Moreover, whereas δ-hydrides are a non-stoichiometric phase with random hydrogen occupancy, DFT calculations model them as stoichiometric structures with a well-defined hydrogen occupancy. This approximation might bias the δ-ZrH$_{1.66}$ into being tetragonal rather than FCC. Since the δ-ZrH$_{1.66}$ structure has consistently been experimentally observed to be FCC, we have averaged the values of the stiffness tensors C_{ij} using

$$C_{11}^{avg} = C_{22}^{avg} = C_{33}^{avg} = (C_{11} + C_{22} + C_{33})/3, \tag{21}$$

$$C_{12}^{avg} = C_{13}^{avg} = C_{23}^{avg} = (C_{12} + C_{13} + C_{23})/3, \tag{22}$$

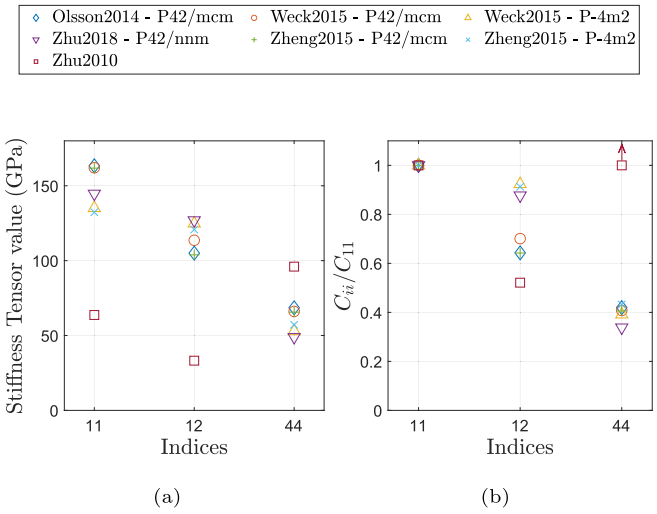

Fig. 2. Different values for the stiffness tensors of the FCC δ-ZrH$_{1.66}$ predicted by DFT calculations [96–100]. (a) shows the averaged values for C_{11}, C_{12}, and C_{44} as provided in the literature and (b) shows the ratios $C_{11}/C_{11}, C_{12}/C_{11}$, and C_{44}/C_{11}. The direction of the subscripts 11, 22, and 33 correspond respectively to the [100], [010], and [001] directions. The range of these values have been used in a sensitivity analysis to study the effect of stiffness tensor values on hydride morphology in Section 3.1.1. The values from Ref. [97] are clear outliers and were not used in this study.

$$C_{44}^{avg} = C_{55}^{avg} = C_{66}^{avg} = (C_{44} + C_{55} + C_{66})/3, \tag{23}$$

where C_{ij}^{avg} represents a stiffness tensor with cubic symmetry. Fig. 2a shows the C_{11}, C_{12}, and C_{44} values of the different averaged stiffness tensors derived from Refs. [96–100].

The direction of the subscripts 11, 22, and 33 correspond respectively to the [100], [010], and [001] directions. Although all the averaged tensors presented in Fig. 2a respect FCC symmetry, discrepancy remains between DFT predictions. The values provided by Zhu et al. [97] are clear outliers and will not be used in the rest of this study. The remaining tensors, however, are still significantly different. These differences can be clearly seen when we normalize the unique components of the stiffness tensor by the 11 component, as shown in Fig. 2b. These DFT predictions thus present significant limitations: the available data offer large variations and correspond to the stiffness tensor value at $T = 0$ K. Based on the values provided in Fig. 2, a sensitivity analysis was performed to understand the effect of the stiffness tensor values on nanoscale hydride shape. This analysis provides insights to guide the choice of stiffness tensor values for the δ-ZrH phase in the phase field model. This study is described below in Section 3.1.1.

Independently of their values, these elastic tensors need to be rotated before being used in the phase field model to ensure that the orientation relationship between the two phases is respected. As stated in Section 1, the orientation relationship between the α-Zr matrix and the δ-ZrH precipitates has been consistently observed to be $\{0001\}_\alpha \| \{111\}_\delta$; $< 11\bar{2}0 >_\alpha \| < 1\bar{1}0 >_\delta$ [2,37,38,40,104]. While the rotation of the stiffness tensors has been overlooked by several studies [49,50,52], it appears to have a significant impact on the nanoscale hydride morphology because of its anisotropy. To ensure that the stiffness tensors of the two phases are accurately aligned to describe the orientation relationship, tensors need to be properly rotated with respect to each other, as shown in Fig. 3.

Due to the symmetry of the two phases, two different arrangements respect the orientation relationship between the face-centered cubic δ-ZrH and hexagonal α-Zr structures, leading to two different hydride variants which differ by a rotation of 60° around the $[0001]_\alpha \| [111]_\delta$ axis. This aspect of the current model differentiates it from previous efforts where the hydride variants came from the eigenstrain description [52,53]. More details on how the rotation matrix and rotation angles can be derived are available in Appendix C.

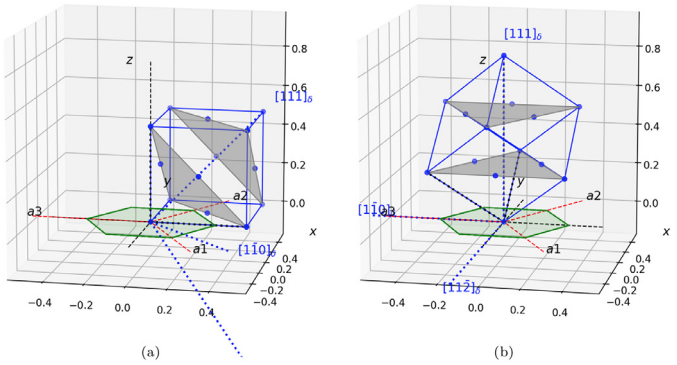

Fig. 3. Rotation of the face-centered cubic δ-ZrH structure with respect to the hexagonal α-Zr structure to respect the orientation relationship between the two phases. The green hexagon represents α-Zr, the blue cube represents the FCC δ-ZrH, the gray triangles represent the $\{111\}_\delta$ planes, and the blue dotted lines represent the $[1\bar{1}0]_\delta, [11\bar{2}]_\delta$, and $[111]_\delta$ directions, which need to align with the $[11\bar{2}0]_\alpha, [\bar{1}100]_\alpha$, and the $[0001]_\alpha$ direction, respectively. (a) shows the arrangement before the rotation, and (b) shows the arrangement after rotation, once the orientation relationship is respected. These figures have been produced using a Python code developed with Jesse Carter from the Naval Nuclear Laboratory. (For interpretation of the references to colour in this figure legend, the reader is referred to the web version of this article.)

Table 4
Eigenstrain tensors for the α-Zr/δ-ZrH$_{1.66}$ system.

Tensor	11	22	33	Ref.
$\epsilon^*_{ij,\delta}$	0.0477	0.0477	0.0745	[12]
λ_{ij}	0.0329	0.0329	0.0542	[105,106]
$\epsilon^{Th}_{ij,\alpha}$ ($\times 10^6$)	5.5	5.5	10.8	[107]
$\epsilon^{Th}_{ij,\delta}$ ($\times 10^6$)	14.1	14.1	14.1	[103]

Eigenstrains: The eigenstrains of the system take into account the different internal anisotropic stress-free strains for the elastic description of the system. In this study, the eigenstrains include three different effects: first, the misfit strain due to the volume difference between the α-Zr phase and the δ-ZrH$_{1.66}$ phase ($\epsilon^{*,mis}_{ij,\delta}$), second, the internal strain due to the presence of hydrogen atoms in solid solution in the hexagonal zirconium matrix ($\epsilon^{*,Hss}_{ij,\alpha} = c_\alpha \lambda_{ij}$ with λ_{ij} the local distortion tensor [105]) and third, the strain due to the thermal expansion of the two phases ($(T - T^{ref}_\alpha)\epsilon^{*,Th}_{ij,\alpha}$ and $(T - T^{ref}_\delta)\epsilon^{*,Hss}_{ij,\delta}$ with T the temperature in Kelvin, and T^{ref}_ν the reference temperature for phase ν). The eigenstrains in the α and the δ phases are thus defined as

$$\epsilon^*_{ij,\alpha} = c_\alpha \lambda_{ij} + (T - T^{ref}_\alpha)\epsilon^{Th}_{ij,\alpha}, \tag{24}$$

and

$$\epsilon^*_{ij,\delta} = \epsilon^{*,mis}_{ij,\delta} + (T - T^{ref}_\delta)\epsilon^{Th}_{ij,\delta}. \tag{25}$$

These physical properties have been measured experimentally or computed numerically and are introduced in the phase field model to accurately describe the elastic contribution.

The anisotropic strain due to the volume misfit between the α-Zr phase and the δ-ZrH$_{1.66}$ phase can be derived from the crystallographic structures. The full derivation can be found in Appendix D. Importantly, the eigenstrain values used in this study listed in Table 4 do not include a shear strain, as supported by Zhang et al. [57] and Louchez et al. [58]. This description differs from the assumptions made in Refs. [52,53], where a large

shear strain of around 19% was added to the models. Although this shear strain was found to be a key aspect of the models from Refs. [52,53], the current work accurately predicts hydride morphology without it.

The strains due to the thermal deformation in both phases are taken from the experimental measurements provided in Refs. [103,107] and are listed in Table 4. The values for the strain in the α-Zr phase due to the presence of hydrogen atoms in solid solution are provided by neutron diffraction measurements performed by MacEwen et al. [105]. It is important to note that the KKS model was chosen over the grand potential model specifically to include the concentration-dependent eigenstrain $\epsilon^{*,Hss}_{ij,\alpha}$ [70]. This concentration-dependent elastic contribution captures the interaction between hydrogen in solid solution and the stress field in the materials, which is crucial to an accurate physical description of the system, as shown in Section 3.

The elastic description of the model accounts for several sources of anisotropy in the system. Due to the high strain created inside and around the nanoscale hydrides, part of the elastic energy is relaxed by plastic deformation [2,11,92–94]. However, this model does not include plastic relaxation. As a result, the model overestimates the magnitude of the elastic strains, stress, and energies predicted in the vicinity of the hydride interface. This approximation is expected to magnify the effect of the elastic energy on hydride shape and interaction.

2.3. Kinetic parameters

A quantitative phase field model must use appropriate kinetic parameters to capture hydrogen diffusion and interface motion. The hydrogen mobility M introduced by the Cahn-Hilliard equation is defined by Kim et al. [59] as

$$M = \frac{D}{f_{cc}}, \tag{26}$$

where D is the isotropic diffusion coefficient of hydrogen described as an Arrhenius law of the type

$$D = D_0 \ \exp\left(-\frac{Q^*_D}{RT}\right), \tag{27}$$

where D is in m^2/s, D_0 is the diffusion coefficient obtained at high temperature in m^2/s, Q^*_D is the activation energy for solid state diffusion of hydrogen in zirconium in J/mol, T is the temperature in Kelvin, and R is the ideal gas constant. The current study relies on the calculations by Zhang et al. [108], which compare well with experimental measurements [3,109,110]. The hydrogen diffusivity depends only slightly on the crystallographic direction in the alloy. Zhang et al. predict that the ratio D_c/D_a of the diffusion coefficients in the a-direction and the c-direction of the hexagonal zirconium is lower than 1.15 for $T < 600$ K [108]. This observation is consistent with other experimental and modeling studies [111,112].

f_{cc} is defined as

$$f_{cc} = \frac{\partial_c^2 f^{\alpha}_{chem} \ \partial_c^2 f^{\delta}_{chem}}{\sum_{\nu}\left[h_{\nu}\prod_{\nu'\neq\nu}\partial_c^2 f^{\nu'}_{chem}\right]} \tag{28}$$

with $\nu = \alpha, \delta_i$ and $\partial^2 f^{\nu}_{chem}/\partial c_{\nu}^2$ written as $\partial_c^2 f^{\nu}_{chem}$ for clarity [59]. Because the chemical free energy density of each phase is described as a parabola and all δ-ZrH variants have the same chemical energy, $\partial^2 f^{\nu}_{chem}/\partial c_{\nu}^2 = \lambda_{\nu}$ and $f^{\delta,i}_{chem} = f^{\delta}_{chem}$. This means that f_{cc} can be simplified as

$$f_{cc} = \frac{\lambda_{\alpha}\lambda_{\delta}}{h_{\alpha}\lambda_{\delta} + h_{\delta}\lambda_{\alpha}}. \tag{29}$$

While hydride precipitation is usually assumed to be a diffusion-controlled phenomenon, recent experimental studies have shown that this transformation transitions from a diffusion-controlled phenomenon at low temperatures to a reaction-controlled phenomenon at high temperatures, with a transition temperature around 580 K [8]. Because most simulations in this study take place at 550 K, the kinetic constant L is defined to be equal to M. This definition has been observed to be sufficient to ensure that hydride precipitation is mostly diffusion-controlled while being computationally efficient.

2.4. Numerical method

Our phase field model is implemented using the finite element method with the Multiphysics Object-Oriented Simulation Environment (MOOSE) [113–116]. Simulations are performed at $T = 550$ K with a total concentration of hydrogen equal to $c_{tot} = 200$ wt.ppm. The temperature of $T = 550$ K was chosen to correspond to the early stages of hydride precipitation. Since hydride nucleation is not included in the model, hydride nuclei are introduced in the domain at $t = 0$ s as circular particles with a radius of 5 nm and with a hydrogen atomic fraction of 0.60, corresponding to a δ hydride. The remaining hydrogen is uniformly distributed in the rest of the domain.

The size of the three-dimensional (3D) domain is limited by the computational cost of the simulations. Most simulations presented in this manuscript require around 250 cores for several weeks. The domain size of the simulations in this study is 100 nm $\times$ 100 nm $\times$ 100 nm. Since the interfacial thickness is fixed at 1 nm for the 3D simulations to resolve the smallest features of the domain, the Cartesian mesh is defined with four or more levels of adaptivity so that a minimum of five elements are present across the interface. These parameters enabled domain sizes on the order of hundreds of nanometers and can be compared to nanoscale hydrides observed experimentally [15]. The time step size starts at 2×10^{-4} ms and an adaptive time stepper readjusts the time step throughout the simulations up to 0.1 ms.

A zero flux is imposed at the boundaries for the variables c and $\vec{\eta}$ to isolate the growing hydrides. The boundary conditions for the displacements are defined to prevent rigid-body motion of the domain while limiting the effect of the boundary conditions on the stress field generated by the hydride. The center of the domain is fixed, and the displacement in the x, y, and z direction is null at the center point of the bottom, back, and left faces of the cubic 3D domain, respectively. To study hydride growth under stress, an applied stress is introduced by applying a pressure on the desired faces of the 3D domain. The pressure corresponds to an applied stress of 250 MPa, unless otherwise specified.

A simulation is considered to have reached equilibrium when the derivative of the total free energy of the system with respect to time provided by Eq. (1) falls below a specified threshold. The threshold value for equilibrium was fixed at $dF_{tot}/dt|_{eq} = 50$ eV/ms.

3. Phase field model predictions of hydride morphology

The phase field model is used to investigate hydride morphology in a single zirconium grain under different precipitation conditions. We first focus on the morphology of a single hydride without applied stress in Section 3.1 and with applied stress in Section 3.2. Then, because mesoscale hydride morphology depends on the stacking behavior of nanoscale hydrides, Sections 3.3 and 3.4 present how hydrides interact and stack, without and with external applied stress, respectively.

3.1. Morphology of a single nanoscale hydride

In Section 2, we defined the phase field model used in this work. The value of the stiffness tensor of the δ-$ZrH_{1.66}$ phase,

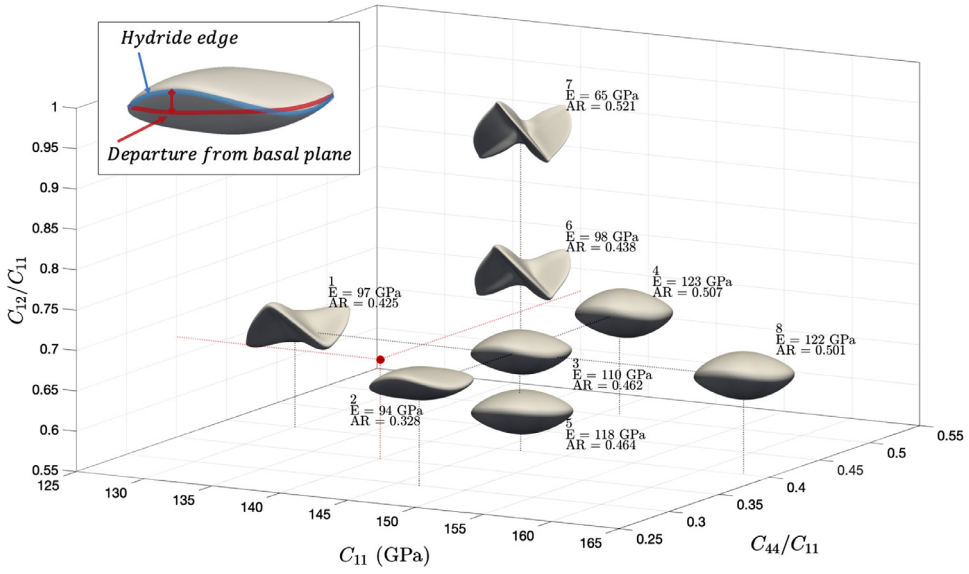

Fig. 4. Effect of stiffness tensor values on nanoscale hydride shape, aspect ratio, and bulk elastic properties. The 3D morphology of nanoscale hydrides is shown for different δ-$ZrH_{1.66}$ phase stiffness tensor values, here characterized by $C_{11}, C_{12}/C_{11}$, and C_{44}/C_{11}. The hydrides are numbered, and the corresponding aspect ratio (AR) of a hydride particle, defined as the ratio between its height and width is specified next to it, along with the effective Young's modulus (E) derived from the stiffness tensor values [98]. The top-left corner image shows how the hydride edge can become wavy and become misaligned with the basal plane. Hydride shape strongly depends on the stiffness tensor values. The stiffness tensor value selected for the rest of this study is marked with a red dot. (For interpretation of the references to colour in this figure legend, the reader is referred to the web version of this article.)

however, was not fixed due to a lack of available data. In Section 3.1.1, we describe how a value was selected for this model. Section 3.1.2 then presents the hydride morphology predicted by the phase field model with the values fixed in the previous section. The effect of a hydride particle on the elastic energy in the matrix and its influence on hydrogen distribution is then described in Section 3.1.3.

3.1.1. Effect of stiffness tensor values on nanoscale hydride morphology

As described in Section 2.2.3, no experimental measurements are available for the δ-$ZrH_{1.66}$ phase stiffness tensor and the current model relies on DFT predictions at $T = 0$ K. Moreover, DFT calculations of the δ-$ZrH_{1.66}$ stiffness tensor offer a wide range of values [96–100]. We performed a parametric study to determine the effect of the stiffness tensor values on the nanoscale hydride shape, aspect ratio, and bulk properties predicted by the phase field model. We then determined which stiffness tensor parameter values should be used in the phase field model. 3D simulations of the growth of single nanoscale hydrides were performed for different values of C_{11} between 130 GPa and 165 GPa, C_{12}/C_{11} between 0.6 and 0.95, and C_{44}/C_{11} between 0.3 and 0.5 to cover the different values presented in Fig. 2. Simulations were performed using MOOSE until equilibrium was reached using the specifications provided in Section 2.4.

As shown in Fig. 4, hydride shape strongly depends on the stiffness tensor values. The final results for the different stiffness tensor values are numbered for identification.

The phase field model predicts the experimentally reported disk-like shape for lower values of C_{12}/C_{11}, but not for other stiffness tensor values. Although the hydride edge lies in the basal plane for high values of C_{11} and C_{44}/C_{11} and low values of C_{12}/C_{11} (see results 3, 5, and 8 in Fig. 4), Fig. 4 shows that the hydride edge becomes wavy for lower C_{11} and C_{44}/C_{11} values and higher C_{12}/C_{11} values (see results 1, 2, 6, and 7 in Fig. 4). This departure from the disk-like shape can lead to complex shapes for higher values of C_{12}/C_{11} and lower values of C_{11} (see results 1, 6, and 7 in Fig. 4). Such complex shapes do not correspond to the hydride shape experimentally observed with TEM and EBSD observations reported in the literature [2,16,40,41,117]. Smaller departures from cylindrical symmetry, however, would not be clearly evident in experimental observations. Moreover, as shown in Fig. 4, the aspect ratio of the disk-like hydrides, defined as the ratio between its height and width, still varies. Hydrides grow more elongated, with smaller aspect ratios, as C_{44}/C_{11} decreases (see changes from result 4 to result 2 in Fig. 4). Fig. 4 also shows the effective Young's modulus of the δ-$ZrH_{1.66}$ phase, which can be derived from C_{11}, C_{12}, and C_{44} using the formula from Ref. [98]. The Young's modulus decreases with decreasing C_{11} and C_{44}/C_{11} values and increasing C_{12}/C_{11} values.

The stiffness tensor values significantly influence the predicted hydride shape and the bulk elastic properties of the δ-$ZrH_{1.66}$ phase, even within the limited range provided by DFT calculations. The choice of stiffness tensor strongly affects phase field modeling predictions. It is important to select stiffness tensor values that lead to reasonable predictions of the nanoscale hydride particle shape. As discussed above, nanoscale hydrides are described as disk-like [2]. This observation justifies selecting a lower C_{12}/C_{11} value. Moreover, nanoscale hydride particles are rather elongated, which corresponds to low aspect ratio values, provided by lower values of C_{11} and C_{44}/C_{11}. Besides, for the δ-$ZrH_{1.66}$ stiffness tensor to represent the elastic properties at $T = 550$ K rather than at $T = 0$ K, the Young's modulus should correspond to experimentally measured values. At $T = 550$ K, the Young's modulus of the δ-$ZrH_{1.66}$ phase was experimentally measured to be between 80 and 107 GPa [15,118–120]. Moreover, the values should be consistent with the majority of the DFT-calculated values presented in Fig. 2. Given these considerations, $C_{11} = 140$ GPa, $C_{12}/C_{11} = 67.5$, and $C_{44}/C_{11} = 0.35$ provide a reasonable hydride shape, aspect ratio, and elastic properties for $T = 550$ K. This value has been marked with a red dot in Fig. 4.

3.1.2. Single hydride morphology

Fig. 5 shows a single nanoscale hydride simulated using the model described in Section 2 with the specific values for the δ-$ZrH_{1.66}$ stiffness tensor that we selected above. Simulations were

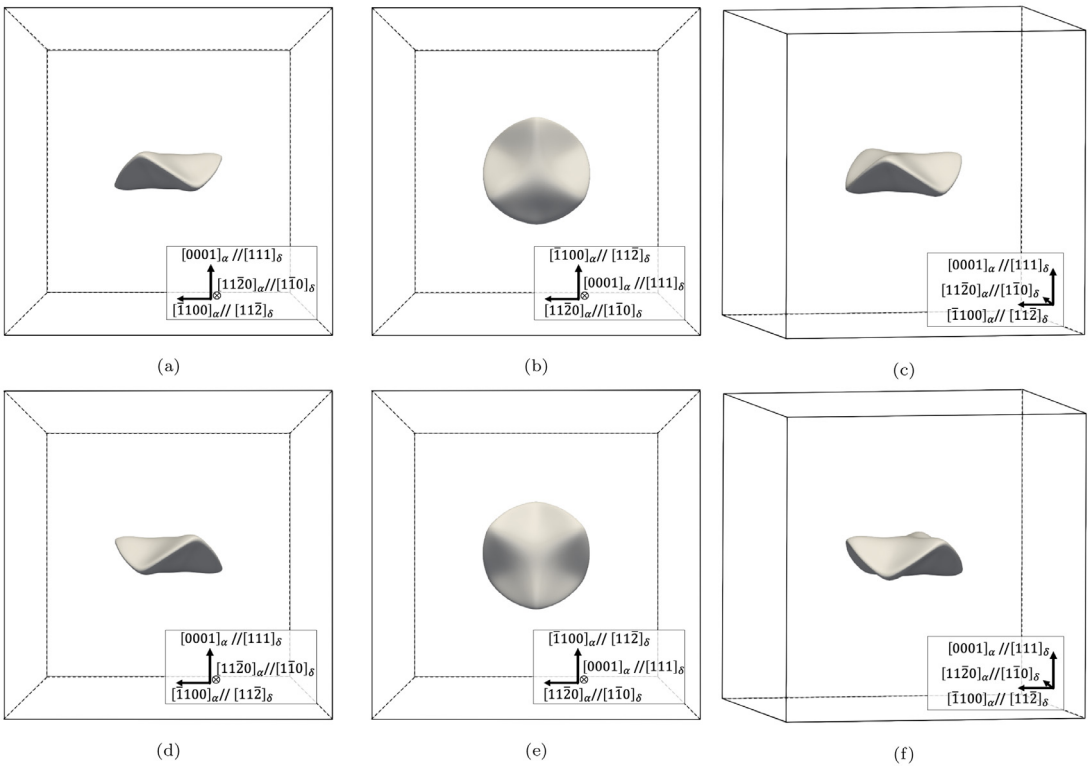

Fig. 5. Nanoscale hydride shape with selected stiffness tensor values of $C_{11} = 130$ GPa, $C_{12}/C_{11} = 67.5$, and $C_{44}/C_{11} = 0.35$ at $t = 1$ ms. This figure shows the two hydride variants from different points of view. (a,b,c) show one variant and (d,e,f) show the other. The two variants differ by a rotation of 60° around the $[0001]_\alpha \| [111]_\delta$ axis. The hydride aspect ratio is equal to 0.359. The domain size is 100 nm × 100 nm × 100 nm.

performed using the specifications provided in Section 2.4. The hydride particle presents an elongated shape along the basal plane of the hexagonal α-Zr matrix with an aspect ratio of 0.359. The Young's modulus is equal to 97 GPa, which falls within the range of experimental values listed above at $T = 550$ K. Remarkably, due to the anisotropy of the stiffness tensor, the nanoscale hydride is not exactly disk-like.

Rather than exhibiting a cylindrical symmetry around the $[0001]_\alpha \| [111]_\delta$ direction, it presents a three-fold rotational symmetry, which corresponds to the three-fold symmetry between the HCP and the FCC structures. As described in Section 2.2.3, the orientation relationship and symmetry of the two crystals lead to two hydride variants. As shown in Fig. 5, the two variants differ only by a rotation of 60° around the $[0001]_\alpha \| [111]_\delta$ axis. This description of the α-Zr/δ-$ZrH_{1.66}$ system will be used in the remainder of this study to investigate nanoscale hydride morphology and stacking behavior.

3.1.3. Influence of a single hydride on the stress field and hydrogen distribution in the matrix

Due to the misfit between the two phases, the matrix is strained to accommodate the growing hydride. Parts of the matrix around the hydride are in compression, and other parts are in tension. The resulting anisotropic stress field in the matrix influences hydrogen distribution, as hydrogen atoms tend to diffuse towards zones in tension to minimize the eigenstrain introduced in Eq. (24). The interaction between the hydrogen in solid solution and the stress field is described as the elastic interaction [121–123]

$$f_{el}^{int,H} = -\sigma_{ij}\epsilon_{ij,\alpha}^{*,Hss}, \tag{30}$$

where $\epsilon_\alpha^{*,Hss}$ is the stress-free strain due to the presence of hydrogen in solid solution in the zirconium matrix introduced in Eq. (24). Zones with positive $f_{el}^{int,H}$ values tend to attract hydrogen atoms. Similarly, the presence of a hydride influences the ability of the matrix to accommodate another hydride particle, as zones in tension can better accommodate the volume change during phase transformation. The energy of this hydride-hydride interaction can be derived as

$$f_{el}^{int,\delta} = -\sigma_{ij}(\epsilon_{ij,\delta}^{*} - \epsilon_{ij,\alpha}^{*}), \tag{31}$$

where the eigenstrains ϵ_δ^* and ϵ_α^* are provided by Eqs. (25) and (24), respectively.

Fig. 6 shows the elastic interaction energies $f_{el}^{int,H}$, $f_{el}^{int,\delta}$, and the hydrogen distribution around a nanoscale hydride. The stress field around the hydride particle is anisotropic and influences hydrogen distribution, hydride growth, and hydride interaction. Zones above and below the hydride platelet are in compression and form hydrogen depleted areas, while zones near the hydride edge are in tension, which attracts hydrogen atoms. Zones in tension also tend to promote hydride precipitation, while zones in compression impede it, leading to the elongated hydride shape. While Section 3.3 specifically focuses on hydride interaction, Fig. 6c provides valuable information on how hydrides are expected to interact. Due to the high elastic interaction energy on top and below the hydride platelet, the stacking of nanoscale hydrides along the $[0001]_\alpha \| [111]_\delta$ direction is probably not energetically favorable. The radial stacking of nanoscale hydrides is thus expected to be unfavorable.

The elastic interactions between the hydrogen in solid solution, the δ-$ZrH_{1.66}$ hydride, and the α-Zr matrix result in the observed hydride shape and hydrogen distribution around the hydride. These elastic interactions are highly sensitive not only to the elastic tensor, as discussed in the previous section, but also to the eigenstrain that results from hydrogen in solid solution and from the lattice mismatch between the two phases. Changes to these elastic inter-

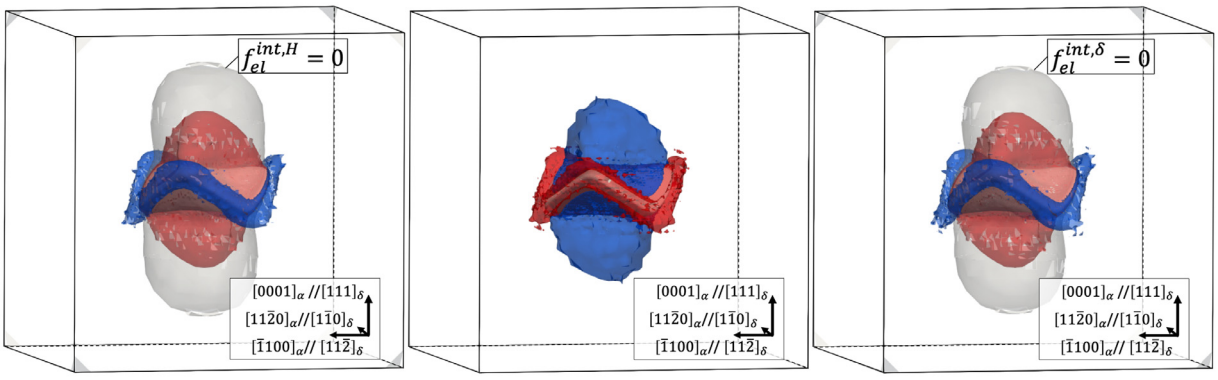

(a) $f_{el}^{int,H}$ (b) Hydrogen distribution (c) $f_{el}^{int,\delta}$

Fig. 6. Effect of the presence of a nanoscale hydride particle on elastic interaction terms and hydrogen distribution. (a) shows the elastic interaction energy $f_{el}^{int,H}$, (b) shows the hydrogen content c, and (c) shows the elastic interaction energy $f_{el}^{int,\delta}$. These images show 3D contours, one for low values (blue), high values (red), and for $f_{el}^{int} = 0$ (gray) when appropriate. Zones on top and below the hydride platelet are in compression and form hydrogen depleted areas, while zones near the hydride edge are in tension and attract hydrogen atoms. The domain size is 100 nm × 100 nm × 100 nm. (For interpretation of the references to colour in this figure legend, the reader is referred to the web version of this article.)

actions are likely to have a significant impact on hydride morphology.

3.2. Effect of applied stress on single hydride growth

As shown in Fig. 5, without applied stress, the hydride shape reflects the three-fold symmetry of the arrangement between the HCP α-Zr and the FCC δ-$ZrH_{1.66}$ phases discussed in Appendix D in Fig. D1. The presence of an applied stress can disturb this symmetry and influence hydride shape. Following the approach described in Section 2.4, we simulate hydride growth to investigate the impact of applied stress on the shape of a single hydride. Fig. 7 shows the predicted hydride shape and its effect on the matrix and hydrogen distribution when precipitation happens under tensile applied stress. Comparing these results with those presented in Figs. 5 and 6 reveals the effect of applied stress on hydride morphology. The morphology depends on the applied load direction, and in both cases, the orientation of the hydride, the shape of the hydride, and the hydrogen distribution around the hydride all change.

As shown in Figs. 7a to 7c, when the stress is applied in the y-direction (in the $[\bar{1}100]_\alpha \| [11\bar{2}]_\delta$ direction), the loss of symmetry due to the applied load causes the hydride to become disk-like and form an angle approximately equal to 35°-40° with the basal plane in the $[\bar{1}100]_\alpha \| [11\bar{2}]_\delta$ direction, which corresponds to the direction of the applied stress. Markedly, its edges have lost the wavy features observed without applied stress in Fig. 5. It is interesting to note that Fig. 7b shows that the hydride grew preferentially in the $[11\bar{2}0]_\alpha \| [1\bar{1}0]_\delta$ direction, i.e. perpendicular to the applied stress. This can be explained by the tension created in the matrix by the applied stress, which modifies the strain field around the hydride and promotes hydride growth in certain directions. As shown in Fig. 7c, the zones around the hydride edges are still in tension and attract hydrogen, and the top and bottom parts are in compression, thus preventing hydrogen agglomeration and hydride growth.

When the stress is applied in the x-direction (in the $[11\bar{2}0]_\alpha \| [1\bar{1}0]_\delta$ direction), as shown in Figs. 7d to 7f, the hydride platelet forms an angle of approximately 20° with the $[\bar{1}100]_\alpha \| [11\bar{2}]_\delta$ direction (i.e. the normal to the hydride disk forms a 20° angle with the $[0001]_\alpha \| [111]_\delta$ direction). In contrast to the hydride obtained with an applied stress along the y-axis, the edges of the hydride shown in Figs. 7d to 7f are still wavy, indicating only a partial loss of symmetry. However, once again, the hydride grows preferentially perpendicular to the direction of the applied stress, i.e. along the $[\bar{1}100]_\alpha \| [11\bar{2}]_\delta$ direction. While the changes in hydride shape and orientation influence the stress field and hydrogen distribution around the hydride particle, the same basic observations remain true. The matrix is in compression below and above the hydride, leading to hydrogen depletion, and the zone near the edge of the hydride is in tension, favoring hydride growth and hydrogen agglomeration.

The applied stress thus influences the stress field in the matrix, which influences hydride shape during growth, which further affects the stress field around the hydride particle. As a result, hydrogen distribution and elastic interaction are affected by the presence of the applied stress. However, it is important to note that in all cases, the top and bottom of the hydride particle are in compression and depleted in hydrogen, while the zone next to the hydride edges is in tension and rich in hydrogen. The difference in the shape of the hydride when the load is applied in the y-direction versus the x-direction can be explained by how the applied stress aligns with the HCP and FCC crystals. The crystal structures shown in Fig. 3 are not equivalent in the different directions of the applied stresses introduced in Fig. 7. Because of the anisotropy of the δ-$ZrH_{1.66}$ stiffness tensor, the delta phase reacts differently when the stress is applied along $[11\bar{2}]_\delta$ or along $[1\bar{1}0]_\delta$. This observation reinforces the importance of properly orienting the two crystals and their elastic tensors to accurately predict the effect of stress on hydride growth.

While Fig. 7 shows results for an applied stress of 250 MPa, a similar shape and loss of symmetry were obtained with applied stresses of 20 MPa, which is much lower than the experimentally observed threshold stresses for hydride reorientation. This change in hydride orientation is thus unlikely to correspond to hydride reorientation at the mesoscale. Rather, the phase field model seems to suggest that in real materials with defects and anisotropic stress field, hydrides are expected to orient more like those shown in Fig. 7 than those shown in Fig. 5.

In light of the results presented here, it is clear that the internal stress state in the zirconium matrix has a significant impact on hydride morphology. The presence of an applied stress breaks the three-fold symmetry of the hydrides and leads to a slight misorientation of the hydride disc with the basal plane of the hexagonal matrix. However, additional hydrides also change the internal stress state and thus may also impact the overall hydride morphology. Therefore, to understand hydride morphology, we need to investigate how nanoscale hydrides interact with each other.

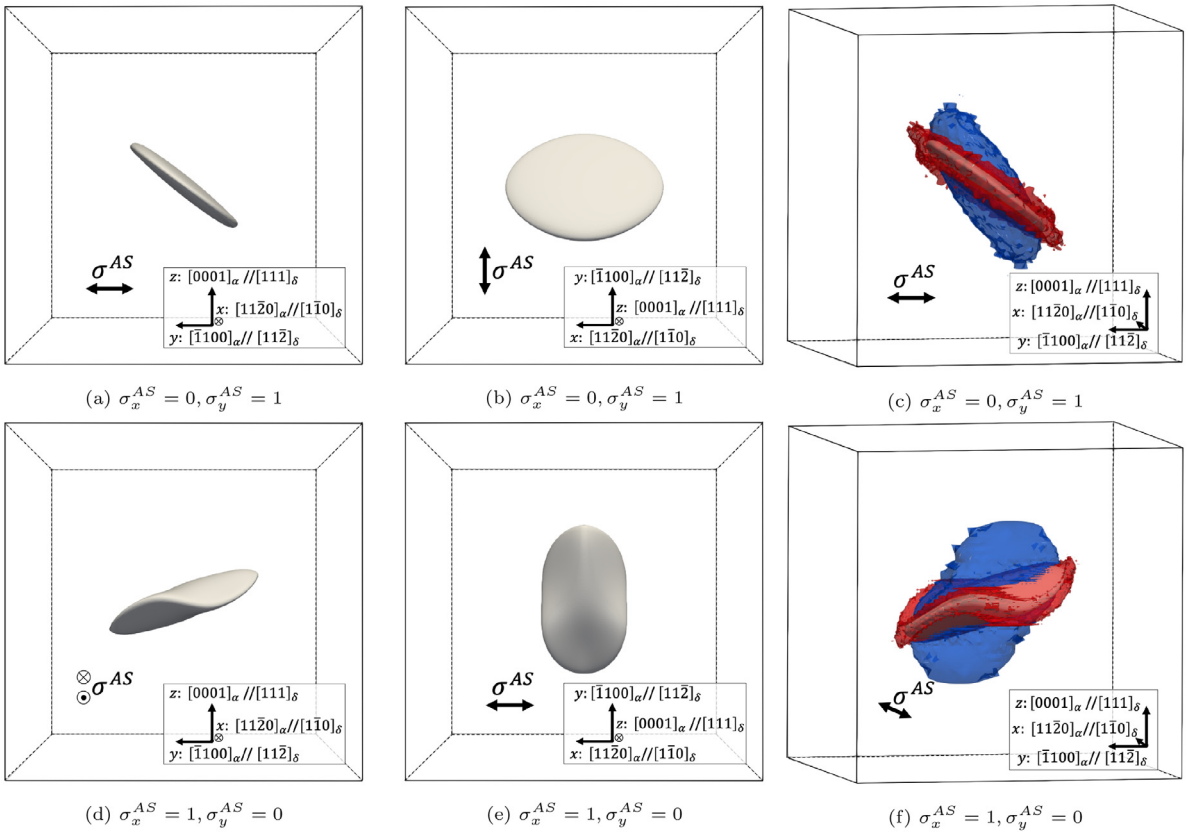

Fig. 7. Effect of a 250 MPa applied stress on hydride shape and orientation. The direction of the applied stress is shown in the figures and is provided by the ratios $\sigma_x^{AS}, \sigma_y^{AS}$ which corresponds to the fraction of applied stress applied in the x and y directions, respectively. (a,b,d,e) show the hydride shape at $t = 1.4$ ms, and (c,f) show the hydrogen distribution around the hydride. The direction of the applied stress influences the shape and orientation of the nanoscale hydride particle and the hydrogen distribution. The results are similar with an applied load of 20 MPa. The domain size is 100 nm × 100 nm × 100 nm.

3.3. Interaction between nanoscale hydrides

The anisotropic strain field generated around nanoscale hydrides not only dictates how hydrides grow and influence hydrogen distribution, but governs hydride interaction as well. The strain fields interact and affect hydride growth, as hydrides arrange themselves in a way that minimizes the total free energy of the system. In this section, we simulate the growth of two neighboring hydride nuclei in different configurations and stacking directions. In Section 3.3.1, both hydrides represent the same variant, while hydrides represent the two different variants in Section 3.3.2. These simulations provide insights into the most favorable or unlikely hydride configurations and stacking directions.

3.3.1. Interaction between hydrides of the same variant

Figure 8 presents how two hydrides from the same variant grow and interact for different initial relative positions. The simulations were performed with the same parameters as in previous sections (see Section 2.4), only this time with two initial hydride nuclei. Spherical hydride nuclei are positioned 30 nm apart either along the $[11\bar{2}0]_\alpha \| [1\bar{1}0]_\delta$, $[\bar{1}100]_\alpha \| [11\bar{2}]_\delta$, or $[0001]_\alpha \| [111]_\delta$ direction and grow under no applied stress. Hydrides interact and influence each other's position, shape, and orientation during growth to minimize the total energy of the system. The behavior of the hydride particles depends markedly on the initial stacking of the nuclei.

In Figs. 8a to 8c, hydrides stacked along $[11\bar{2}0]_\alpha \| [1\bar{1}0]_\delta$ misalign themselves with the basal plane by rotating together around the same axis. They are attracted to each other as they grow, until they merge into one single hydride. The resulting hydride exhibits a similar disk-like shape and orientation as the hydrides observed in Figs. 7a to 7c under applied stress. In Figs. 8d to 8f, hydrides stacked along $[\bar{1}100]_\alpha \| [11\bar{2}]_\delta$ attract each other, rotating around parallel axes. They elongate towards each other and take on a similar shape and orientation as shown in Figs. 7d ti 7f. However, in this configuration, hydrides align in the $[\bar{1}100]_\alpha \| [11\bar{2}]_\delta$ direction without merging. They rotate around the $[11\bar{2}0]_\alpha \| [1\bar{1}0]_\delta$ direction, which misaligns their edges and prevents them from merging. In the case of the stacking along the $[0001]_\alpha \| [111]_\delta$ direction shown in Figs. 8g to 8i, hydrides repel each other along the $[0001]_\alpha$ direction, before taking on the disk-like shape and orientation observed previously in Figs. 7a and 8c and leaving their $[0001]_\alpha$ stacking direction.

These three configurations show that the initial hydride stacking influences hydride interaction. They can merge, repel each other, or align without merging. Explaining these behaviors requires investigating the elastic interaction energy between hydrides introduced in Eq. (31). Fig. 9 shows $f_{el}^{int,\delta}$ on 2D slices of the simulations presented in Fig. 8. As explained above, negative values of elastic interaction energy promote hydride growth, while positive values impede it [123]. Zones with negative values are located near the edges of the hydride particles, while positive values are located above and below them. Fig. 9a shows that the elastic interaction energy is negative between the two hydrides for the $[11\bar{2}0]_\alpha \| [1\bar{1}0]_\delta$ stacking. Thus, there is a driving force for the hydrides to merge and form a single hydride. When the elastic interaction energy is positive between the two hydrides, there is no driving force for them to merge. Fig. 9b shows that the two hydrides align with a distance that optimizes the elastic interaction for the $[\bar{1}100]_\alpha \| [11\bar{2}]_\delta$ stacking. The positive elastic interaction en-

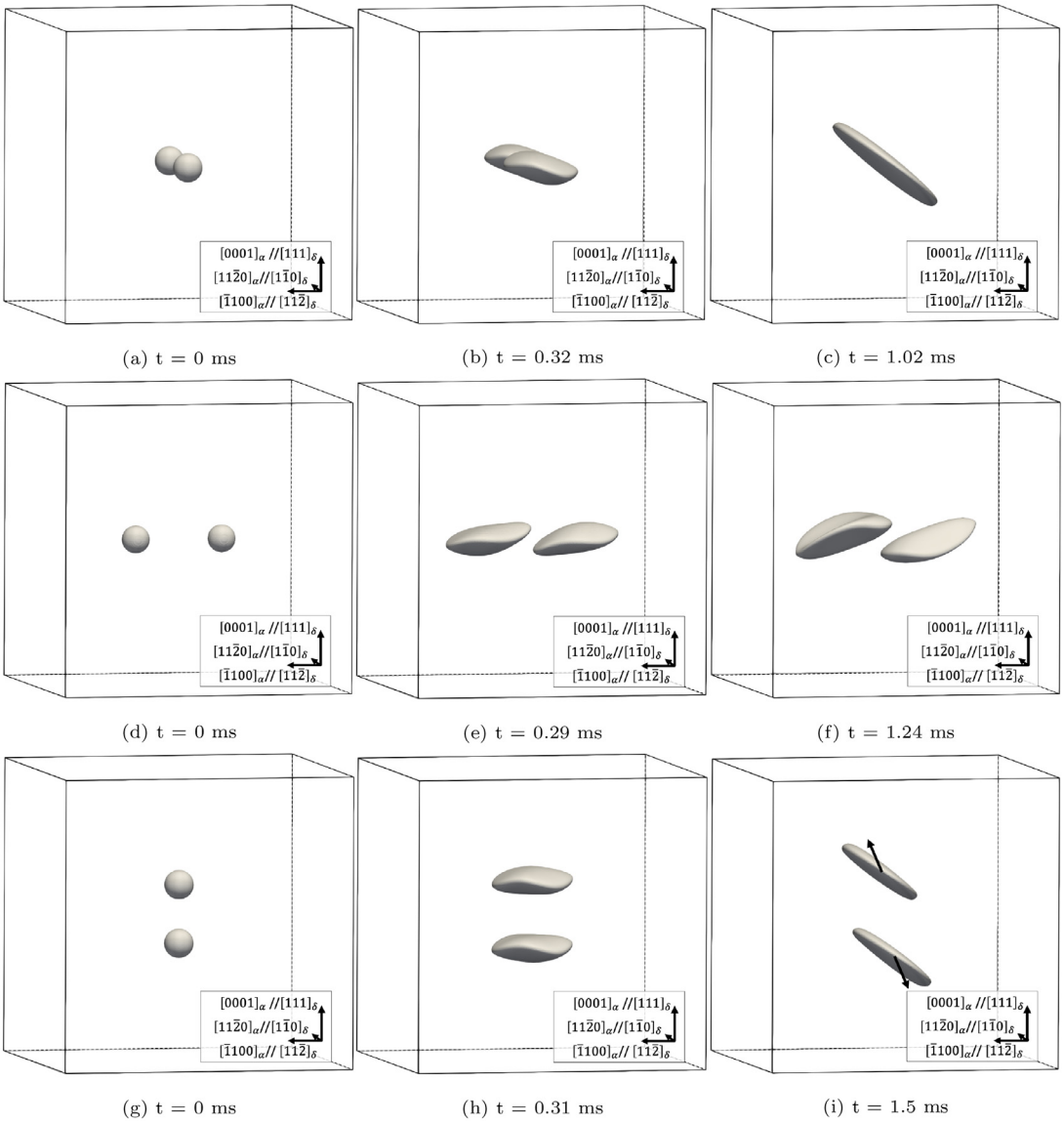

Fig. 8. Hydride interaction during growth when both hydrides represent the same variant. Two spherical hydride nuclei are positioned close to each other either along the $[11\bar{2}0]_\alpha \| [1\bar{1}0]_\delta$ (a,b,c), $[\bar{1}100]_\alpha \| [11\bar{2}]_\delta$ (d,e,f), or $[0001]_\alpha \| [111]_\delta$ (g,h,i) direction and grow without applied stress. Hydrides interact and affect each other's position, shape, and orientation to find the most favorable configuration given the initial positions. In (a,b,c), the hydrides merge together, in (d,e,f), they align along the $[11\bar{2}0]_\alpha \| [1\bar{1}0]_\delta$ direction without merging, and in (g,h,i), they repel each other along the $[0001]_\alpha$ direction. The domain size is 100 nm × 100 nm × 100 nm.

ergy between them prevents them from merging. However, having them further away from each other would create an area with negative elastic interaction energy, which would act as a driving force to bring them closer. When the elastic interaction energy is too large, however, hydrides repel each other. This is the case for the $[0001]_\alpha \| [111]_\delta$ stacking, shown in Fig. 9c. Hydrides are in the compression zones created by the other hydride and the elastic interaction energy is high. They thus repel each other along the $[0001]_\alpha$ direction to find a more favorable configuration. The configuration shown in Fig. 8i is not at equilibrium. The hydrides are slowly translating further away from each other in the $[\bar{1}100]_\alpha \| [11\bar{2}]_\delta$, $[0001]_\alpha \| [11\bar{2}]_\delta$, and $[0001]_\alpha \| [111]_\delta$ directions. In the meantime, the top hydride is dissolving and the bottom hydride is growing to minimize interaction. The selection of one particle over the other is attributed to random numerical fluctuations.

The translation of the hydrides away from the $[0001]_\alpha \| [111]_\delta$ stacking direction means that another configuration is more favorable. To find this configuration, two hydride nuclei were positioned 26 nm apart in the $[0001]_\alpha \| [111]_\delta$ and 20 nm apart in the $[\bar{1}100]_\alpha \| [11\bar{2}]_\delta$ direction, as shown in Fig. 10. Except for the initial position of the hydride nuclei, the simulation is the same as those shown in Fig. 8. Hydrides quickly take on the same shape already observed in Figs. 7c,8c and 8i, and then align themselves in the direction of the elongation to minimize elastic interaction.

The relative stability of the configurations shown in Fig. 8 and 10 can be established by comparing the total free energies of the systems. This will be done at the end of the next section in Section 3.3.3 after studying the configurations for hydrides from different variants.

3.3.2. Interaction between the two different hydride variants

Due to the different crystal orientations of the two hydride variants, two hydride particles interact differently when they represent different variants. Fig. 11 shows how the two hydride variants interact. Simulations were performed with the same parameters as in Fig. 8, except that each hydride nuclei represent one of the two hydride variants.

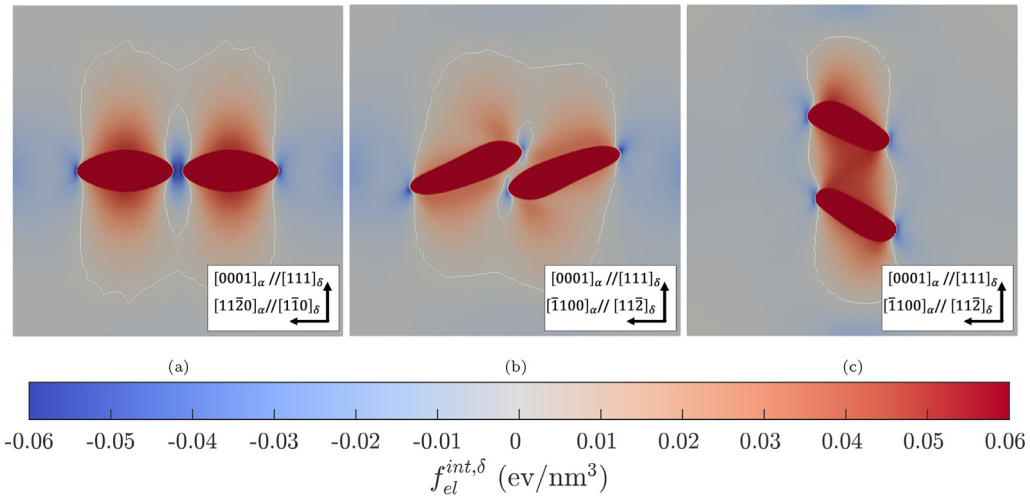

Fig. 9. Elastic interaction $f_{el}^{int,\delta}$ between hydrides from the same variant when stacked along the (a) $[11\bar{2}0]_\alpha \| [1\bar{1}0]_\delta$, (b) $[\bar{1}100]_\alpha \| [11\bar{2}]_\delta$, and (c) $[0001]_\alpha \| [111]_\delta$ directions at respectively $t = 0.24$ ms, $t = 1.24$ ms, and $t = 1.25$ ms. The white line shows the contour for $f_{el}^{int,\delta} = 0$ ev/nm^3. In (a), the elastic interaction energy is negative due to the large tensile stress present at the edges of the hydrides, leading to the two hydrides merging. In (b), the elastic interaction energy is positive between the two hydrides and they keep each other at a set distance where the elastic interaction term is null. In (c), the elastic interaction term is positive between the two hydrides and they repel each other. The domain size is 100 nm × 100 nm × 100 nm.

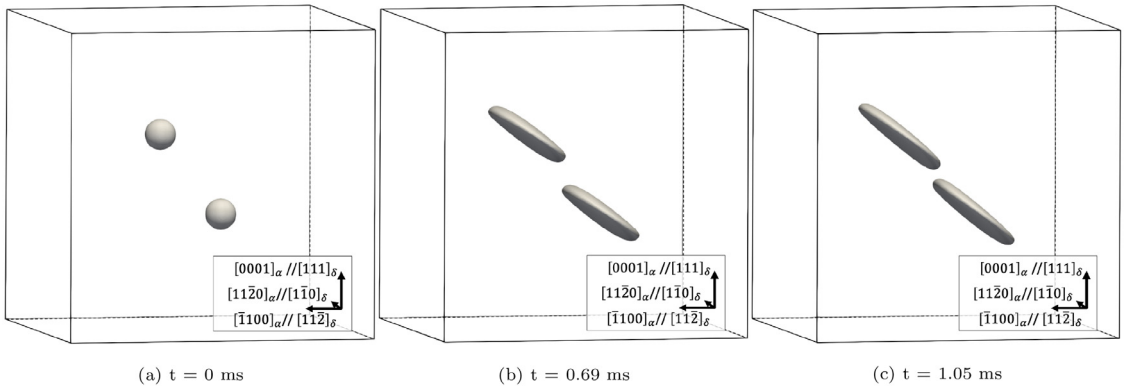

Fig. 10. Hydride interaction during growth when both hydrides represent the same variant. Two spherical hydride nuclei are positioned close to each other, 26 nm apart in the $[0001]_\alpha \| [111]_\delta$ direction and 20 nm apart in the $[\bar{1}100]_\alpha \| [11\bar{2}]_\delta$ direction and grow without applied stress. Hydrides interact and affect each other's position, shape, and orientation to find the most favorable configuration given the initial positions. In this case, hydride particles stack along the elongated direction, forming an angle of around 40° with the basal plane of the hexagonal matrix. The domain size is 100 nm × 100 nm × 100 nm.

When hydrides of different variants are stacked along $[11\bar{2}0]_\alpha \| [1\bar{1}0]_\delta$, they misalign themselves with the basal plane by rotating around the same axis and take on the shape and orientation previously observed. However, because they represent two different variants, they rotate in opposite directions, as shown in Fig.. This results in the two hydrides forming an X in the $(11\bar{2}0)_\alpha$ plane as they come in contact. Because these two hydrides represent different variants, a grain boundary separates them when they touch. In Fig., hydrides stacked along $[\bar{1}100]_\alpha \| [11\bar{2}]_\delta$ attract each other. They grow elongated towards each other and come in contact. This configuration differs from the one observed in Fig. where hydrides represented the same variant. Rather than stacking without merging due to the positive elastic interaction term between them, the two hydrides merge and form a V shape. In the case of the stacking along the $[0001]_\alpha \| [111]_\delta$ direction shown in Fig., hydrides repel each other along the $[0001]_\alpha$ direction, before one of them takes on the disk-like shape and orientation observed previously, while the other starts dissolving.

The last two sections have shown how nanoscale hydrides interact and stack depending on their initial relative positions and the variants being represented. The basic mechanisms between hydride particle interaction can be explained using the elastic interaction energy $f_{el}^{int,\delta}$. Hydrides interact to minimize the elastic interaction energy. When $f_{el}^{int,\delta}$ is positive between the hydrides, they repel each other. When $f_{el}^{int,\delta}$ is negative, this promotes hydride growth and hydrides tend to merge. Interestingly, very different stacking behaviors result from these mechanisms depending on the initial hydride configuration. The following section compares the energy of these morphologies to determine which ones are the most favorable.

3.3.3. Stability of nanoscale hydride stacking

The previous sections have shown that neighboring hydrides interact with each other and influence each other's shape, orientation, and position. Different hydride morphologies were obtained depending on the initial hydride configurations. The relative stability of these configurations can be established by comparing the total free energies of the systems.

The stackings along the $[11\bar{2}0]_\alpha \| [1\bar{1}0]_\delta$ direction (x-axis) are some of the most stable ones. When both hydrides represent the same hydride variant, as shown in Fig. 8a, the stacking along the x-axis allows the hydrides to break the three-fold symmetry observed in Fig. 5 and to merge as one hydride. As shown in Fig. 12a, these events significantly decrease the total free energy of the sys-

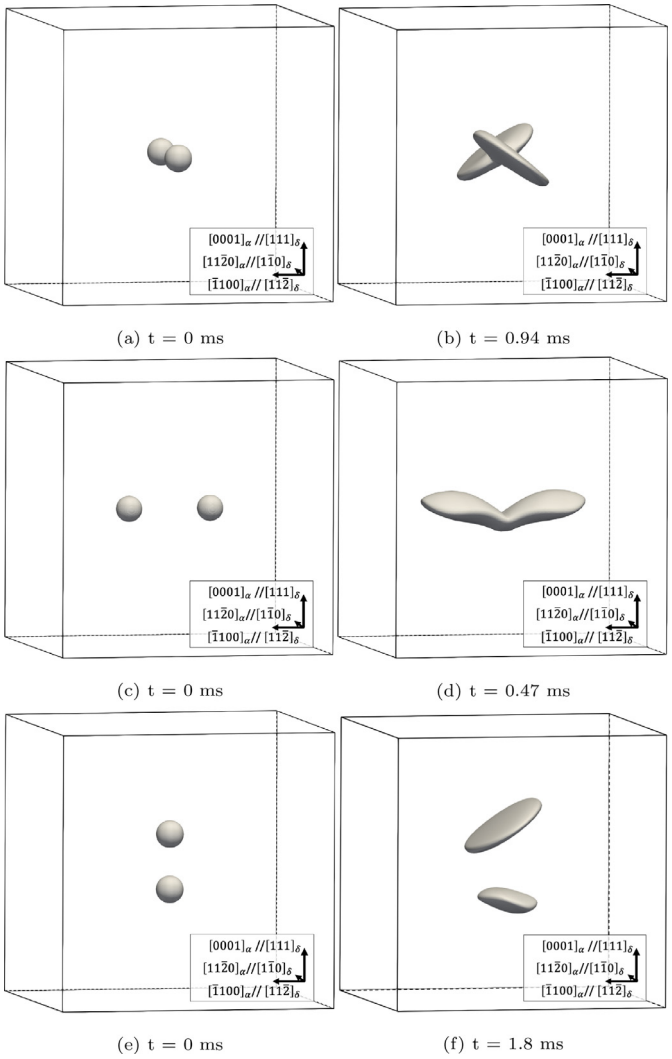

Fig. 11. Hydride interaction during growth when both hydrides represent different variants. Two spherical hydride nuclei are positioned close to each other either along the (a,b) $[11\bar{2}0]_\alpha \| [1\bar{1}0]_\delta$, (c,d) $[\bar{1}100]_\alpha \| [11\bar{2}]_\delta$, or (e,f) $[0001]_\alpha \| [111]_\delta$ direction and grow without applied stress. Hydrides interact, affect each other's position, shape, and orientation to find the most favorable configuration given the initial positions. In (a,b), because each variant selects a different orientation, the two hydrides come in contact to form an X. In (c,d), the two hydride variants come in contact to form a V shape. In (e,f), they repel each other along the $[0001]_\alpha$ direction. The domain size is 100 nm × 100 nm × 100 nm.

tem at around $t = 0.4$ ms, leading to the most favorable configuration. When the two hydrides represent different variants, as in Fig. 11a, the change in orientation and the contact between the two hydrides also significantly reduces the total free energy of the system at around $t = 0.4$ ms.

The stackings along the $[\bar{1}100]_\alpha \| [11\bar{2}]_\delta$ direction (y-axis), both with one and two variants, shown in Fig., leads to stable configurations in which two distinct hydrides stack along the basal plane. However, despite their stability, these configurations are not the most favorable, as shown in Fig. 12a.

The initial stacking along the $[0001]_\alpha \| [111]_\delta$ direction (z-axis) was shown to be unstable in Figs. 8, 11. Hydrides repel each other to find a more stable configuration to minimize the total free energy of the system. In Fig. 8i, by changing their orientation and growing away from a $[0001]_\alpha$ stacking into a more aligned position, the two hydrides found a more stable configuration, as shown by the drop in total free energy in Fig. 12a. In Fig. 11f, one of the hydrides dissolves to minimize elastic interactions and promote the growth of the resulting hydride. While the $[0001]_\alpha$ stacking had a higher total free energy than the $[\bar{1}100]_\alpha \| [11\bar{2}]_\delta$ stacking, the later hydride arrangements present similar energies and are thus almost as favorable.

Aligning the initial hydride in the y-z direction as shown in Fig. 10 allows the hydrides to find a favorable configuration that remains stable for a while. While not as energetically favorable as a stacking along the $[11\bar{2}0]_\alpha \| [1\bar{1}0]_\delta$ direction (x-axis), this configuration is more favorable than a stacking in the $[\bar{1}100]_\alpha \| [11\bar{2}]_\delta$ direction (y-axis). Hydrides then merge to further reduce the total free energy of the system.

In general, the contribution from the chemical energy is the largest and is dominant over the elastic and interfacial contributions. However, the elastic energy has a clear impact on hydride shape and interaction. Contrasting Fig. 12b and Fig. 12c shows that hydride precipitation is initially driven by the chemical energy rather than the elastic energy. The elastic energy increases significantly at first, indicating little impact. However, the elastic energy then starts significantly impacting hydride shape and orientation and decreases as the system minimizes the total free energy of the system. The elastic contribution can also indirectly prevent hydride growth, which keeps the chemical energy high in some cases. The interfacial energy, however, is small enough to have little impact. As shown in Fig. 12d, it even increases significantly as hydrides find the most stable configurations.

3.4. Effect of applied stress on hydride interactions

Previous sections have shown that the hydride shape presented in Fig. 5 is influenced by the presence of applied stress or other hydrides, as shown in Figs. 7, 8 and 11. Depending on the stacking direction or the direction of the applied stress, the hydrides tend to orient in two different ways shown in Figs. 7a and Figs. 7d. The effect of the initial hydride stacking and the applied stress can either complement each other or compete. For example, in the case of a stacking along $[11\bar{2}0]_\alpha \| [1\bar{1}0]_\delta$ with an applied stress along $[\bar{1}100]_\alpha \| [11\bar{2}]_\delta$, the two promote the same hydride orientation. If the hydrides are stacked along the direction of the applied stress, the two configurations are then expected to compete.

However, performing the simulations of hydride interaction under an applied stress of 250 MPa did not lead to different hydride morphologies than without stress, which were shown in Figs. 8 and 11, nor to a change in the relative stability of the different hydride configurations. Since we observed no significant change, we do not show the results from our simulations with applied stress. Despite the competing effect of an applied load of 250 MPa, hydride shape and orientation were governed by hydride interaction. Hydride shape and orientation were not noticeably influenced by the presence of an applied stress, which appears negligible compared to the effect of the presence of a secondary hydride. The stacking of hydrides along $[0001]_\alpha$ remains unfavorable with or without applied stress due to the elastic interactions between hydride particles. Hydride reorientation as a change in nanoscale hydride stacking under applied stress is thus not accounted for in the current phase field simulations.

4. Comparison against experimental observations

In this section, we compare the predictions made by the phase field model against experimental observations. Because the current study focuses on hydride precipitation in single grains, it is important to compare its predictions with experimental observations of intragranular hydride precipitation in large grains. Zirconium hydride samples have been prepared following the process described in Appendix E to complement published microstructures [16,40,117]. The samples were recrystallized to obtain large

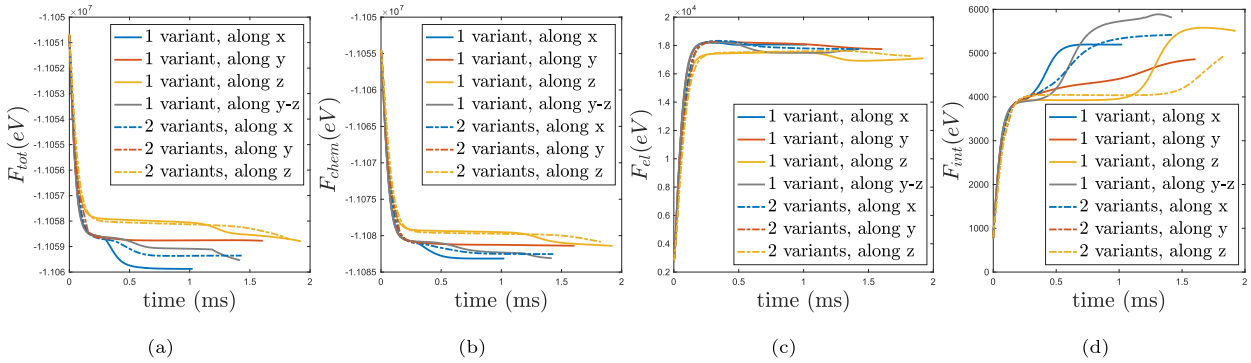

Fig. 12. Evolution of the free energies during hydride growth for the different hydride configurations shown in Figs.. The total free energy F_{tot} shown in (a) is decomposed into the chemical free energy (b), the elastic free energy (c), and the interfacial free energy (d). While the reduction of the chemical free energy is the main driving force for hydride precipitation, the elastic and interfacial free energies govern hydride shape and orientation. Configurations with a lower total free energies are more stable. Hydride stacking along the x direction ($[11\bar{2}0]_\alpha \| [1\bar{1}0]_\delta$) appear to be the most stable, closely followed by the diagonal alignment shown in Fig. 10, referred to as the alignment along y-z. Stacking along the y direction ($[\bar{1}100]_\alpha \| [11\bar{2}]_\delta$) are not as favorable, but stackings along the z direction ($[0001]_\alpha \| [111]_\delta$) are the least favorable until they change to another stacking direction.

grains, i.e. conditions closer to the single grain conditions simulated in this study. The microstructure showing several nanoscale hydrides in large zirconium grains is presented in Fig. 13a, which, along with published microstructures, can be qualitatively compared with the simulation results presented in this study. A quantitative comparison is made challenging by the difference in scale between the phase field predictions and the experimental results, which is discussed in Section 5, and the lack of information on the crystallographic orientation on the experimental images.

As discussed above, the morphology of an isolated hydride in a perfect single crystal without applied stress presented in Fig. 5 is unlikely to be observed experimentally. A small applied stress of 20 MPa was shown to be enough to break the hydride symmetry and lead to a change in hydride shape and orientation. In a real material, residual stresses, grain boundaries, other particles, defects, and other imperfections are expected to break this symmetry and hydrides are more likely to appear as shown in Figs. 7, 8 and 11. The phase field model thus predicts that in real materials, even isolated hydride particles are thin and elongated. In Fig. 13a, like in the literature [2,15], some of the more isolated hydrides indeed appear as thin, elongated particles, like the model predicts. However, hydride particles are rarely isolated. They are often observed to grow next to each other and stack.

The current phase field model predicts several possible hydride morphologies and stacking behavior depending on the configuration of hydride nuclei. These stacking behaviors have also been observed experimentally. For example, the stacking behavior predicted in Fig. 10c corresponds to experimental observations presented in Fig. 13. Fig. 13 shows a 2D slice of the simulation results from Fig. 10c alongside experimental observations of stacking hydrides. In both experimental observations and simulation predictions, elongated hydride particles stack to form a longer mesoscale hydride. Hydride tips are slightly misaligned, which prevents them from merging, and gives the mesoscale hydrides a slightly different orientation relative to the matrix crystallography than that seen in the nanoscale hydrides.

The other stacking behavior predicted by the phase field model, presented in Fig. 8f, corresponds better to a TEM observation shown in Fig. 14a. A dark field image using hydride reflection reveals less regular hydrides stacking with greater overlap than in Fig. 13. The 2D slice from Fig. 8f shows a similar stacking behavior to that observed experimentally in Fig. 14a. The peanut-like hydride shape, the overlap, and the angle between the hydride orientation and the orientation of the stacking direction are all similar.

Hydride stacking of several variants has also been observed experimentally by Perovic et al. [40,117]. The TEM images presented in Fig. 15 show hydrides with different orientations forming angles between 50° and 120°. The discrepancy in the measured angle formed by the two hydride variants has not been fully understood. Perovic offered some arguments in favor of elastic strains and elastic interactions between hydride platelets to explain these stacking behaviors [117]. It is also possible that the interfacial energy terms, plasticity dissipation mechanisms, or other mechanisms are at play here. However, the behavior predicted by the phase field model, which includes the anisotropic elastic strains and elastic constants, seems to explain these observations.

These experimental observations can be compared with the phase field predictions presented in Fig. 11, where stacking of the two hydride variants was observed. While only two different stacking behaviors were predicted, one forming an X shape and another forming a V shape, these morphologies can account for the different angles formed between hydrides observed experimentally. As shown in Figs. 15d to 15h, the measured angle between the two hydride variants forming an X varies between 60° and 180° depending on the plane of observation. Because experimental observations only provide 2D representations of a 3D hydride configuration, the different stacking behaviors observed experimentally could all originate from the configuration predicted by the phase field model shown in Fig. 11b. The V shape formed by the two hydrides variants stacked along the $[\bar{1}100]_\alpha \| [11\bar{2}]_\delta$ forms an angle of around 145°, as shown in Fig. 15i, which is also similar to the configuration observed experimentally. Since experimental observations seem to be reproduced at least qualitatively by the phase field model presented in this study, other mechanisms not included in the model are believed to have secondary effects.

Although the predicted angles do not correspond exactly to the values reported by Perovic et al. [40,117] (50°-120° vs. 60°-180°), the disparity can reasonably be explained by three facts. First, although every angle from $\theta = 60°$ to $\theta = 180°$ can be observed, the chance of observing the hydrides forming a specific angle θ_0 decreases as θ_0 increases. In other words, there is a bias towards the observation of lower values of θ due to the hydride morphology. Assuming that the plane of the experimental observation randomly falls on one of the planes shown in Figs. 15d to 15h, which uniformly cover the possible planes, the reported angle is three times more likely to fall within the 60°-120° range than within the 120°-180° range. Secondly, hydride variants aligning with an angle close to 180° might have been indistinguishable from a single hydride. Such high angles might thus not have been reported, thus further biasing the report of lower angles. Finally, the current model does

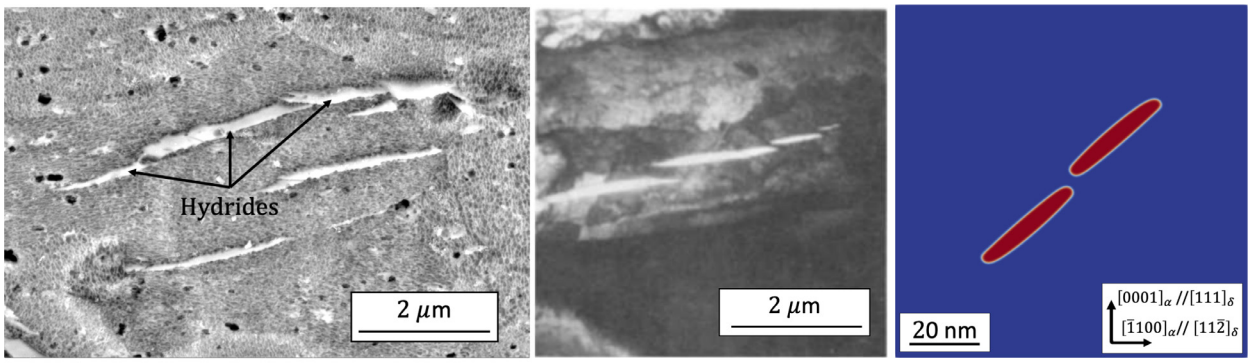

Fig. 13. Experimental observations of hydrides at high magnitude and comparison with phase field prediction. (a) is an SEM Image of hydrides in a sample containing a total of 200 wt ppm of hydrogen. Courtesy of Evrard Lacroix. This image was taken using an FEI Helios Focused Ion Beam microscope in scanning electron microscope (SEM) mode. Sample preparation and imaging are described in Appendix E. It shows the nanoscale hydride stacking circumferentially in a large α-Zr grain. (b) shows an inclined stack of parallel hydrides in pure Zr containing 30 wt.ppm of hydrogen captured using TEM [117]. (c) shows a 2D slice of the stacking behavior observed in Fig. 10c at $t = 1.05$ ms. The phase field predicted hydride stacking behavior corresponds to experimental observations.

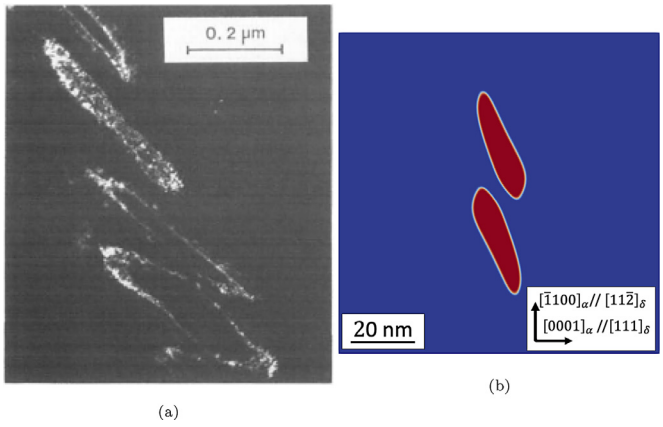

Fig. 14. Experimental observations of hydrides at high magnitude and comparison with phase field predictions. (a) shows the stacking of nanoscale hydrides in a TEM dark field image using hydride reflection [40], which is similar to the stacking behavior predicted by the phase field model as shown in (b). (b) is a 2D slice of the modeling results presented in Figs. 8d to 8f at $t = 1.24$ ms. Both experimental observations and modeling results show overlapping peanut-shaped hydrides.

not account for the anisotropic interfacial energy of the system, which, as is discussed in Section 5, could affect the orientation of the hydride with respect to the basal plane. If the anisotropic interfacial energy were to decrease the orientation of the hydride with respect to the basal plane from 30° to 25°, then the smallest predicted angle between the two hydride particles shown in Fig. 15d would become 50° and correspond to experimental observations.

The phase field predictions concerning hydride shape and stacking behaviors have been compared against experimental observations of hydride morphology obtained without applied load. Although our simulation domain is smaller than the size of the experimental microstructures due to the large computational cost of the 3D simulations, similar results are expected to be obtained in larger simulation domains. This is because hydride orientation, shape, and interaction are driven by elastic energy, which would scale with domain size. These comparisons thus support the hypothesis of this work stating that the anisotropy of the elastic properties of the α-Zr and δ-$ZrH_{1.66}$ phases is primarily responsible for the observed stacking behavior of nanoscale hydrides. The phase field model accounts for the observed elongated shape of nanoscale hydrides and their stacking behavior. Moreover, these phenomena are attributed to the anisotropy of the elastic properties of the α-Zr/δ-$ZrH_{1.66}$ system. The model can also explain some of the disparities between experimental observations. Differences in observed hydride morphology at the lower scales might be due to differences in hydride stacking direction or the different hydride variants involved, as shown in Figs. 13 to 15.

However, the current version of phase field model cannot account for stress induced hydride reorientation. As explained in Section 1, an applied tensile stress between 55 and 240 MPa has been experimentally observed to cause hydride reorientation, where nanoscale hydrides stack radially rather than circumferentially in the zirconium cladding. Although this model accounts for some changes in single hydride shape and orientation under applied load, it does not predict any significant changes in hydride stacking behavior, even for an applied stress of 250 MPa. This is in contradiction with experimental studies, which, as presented in Section 1, observe reorientation at the mesoscale for tensile stresses between 55 and 240 MPa.

5. Discussion

In this study, we used phase field modeling to study nanoscale hydride morphology in a single crystal. This work aims to determine the mechanisms governing hydride morphology with and without external applied stress. In particular, we hypothesized that the anisotropy of the elastic properties of the α-Zr/δ-ZrH system and the zirconium grain structure play a significant role in hydride morphology. Therefore, the quantitative phase field model developed in this work includes many sources of anisotropy in the elastic contribution to the α-Zr/δ-ZrH system. This phase field model differs from previous efforts in several ways. For example, the rotation of the stiffness tensors to respect the orientation relationship is particularly unique. Moreover, the quantification of the effect of the variations in DFT calculations of the δ-ZrH stiffness tensor on phase field model predictions is also novel. Due to a lack of data on the value of the δ-$ZrH_{1.66}$ phase stiffness tensor at high temperature, the phase field predictions were compared for different stiffness tensor values. It appears that hydride shape and orientation strongly depend on the elastic properties of the two phases. The particular attention paid to the stiffness tensor orientation, symmetry, and values in this study differentiates it from previous studies [48,50–53,56,124]. We assumed a specific value for the δ-$ZrH_{1.66}$ phase stiffness tensor based on the measured Young's modulus, on the aspect ratio of a single hydride, and consistency with the majority of the DFT-calculated values. Future work is needed to obtain a more accurate value for the stiffness

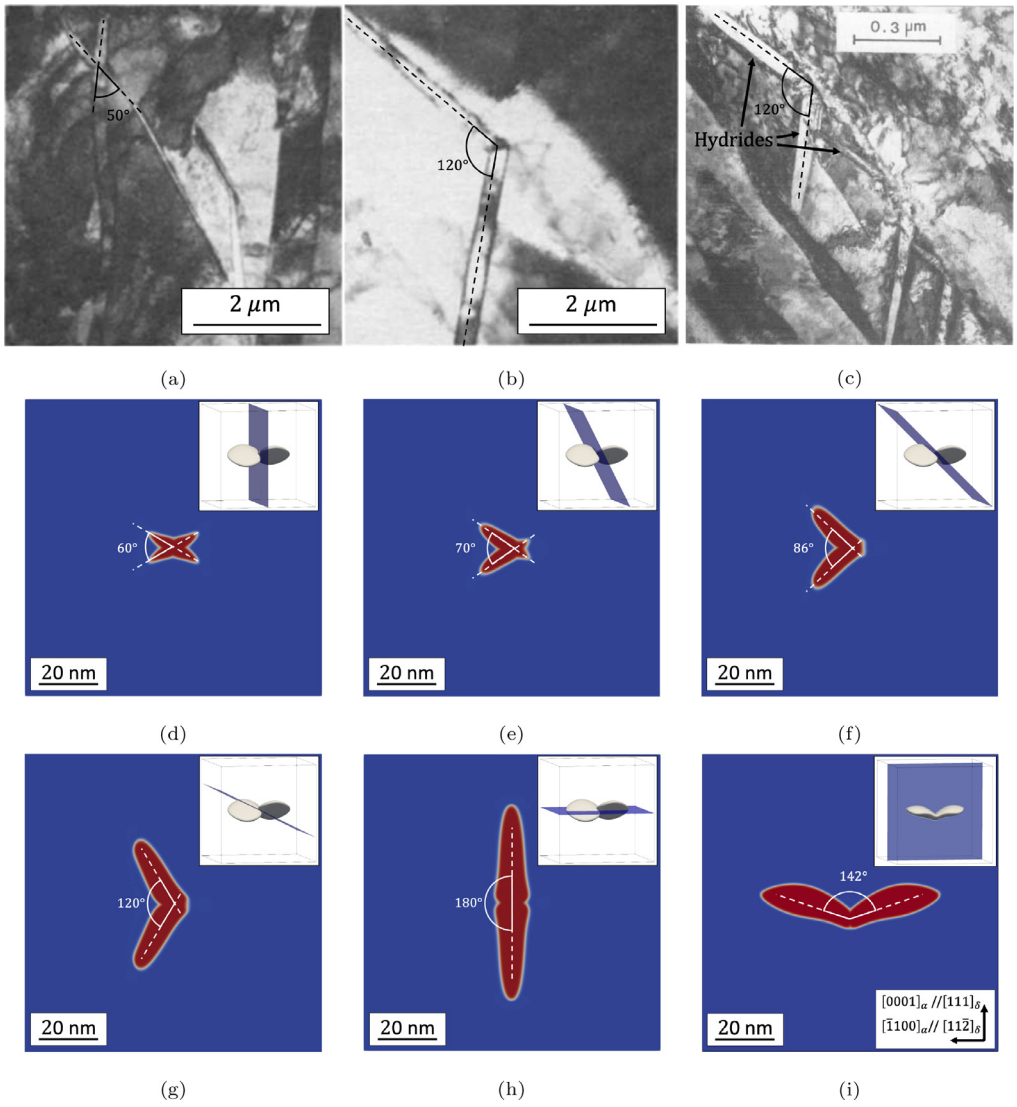

Fig. 15. Experimental observations of hydrides at high magnitude and comparison with 2D slices of the configurations predicted by the phase field model. (a,b,c) shows the stacking of different nanoscale hydride variants in TEM images [40,117], where different angles can be measured between hydride variants. (d,e,f,g,h) show 2D slices of the modeling results presented in Fig. 11b along different planes shown in blue on the top right corner of each image, and (i) show a 2D slice of the modeling results presented in Fig. 11d. The measured angle between the hydride variants in the X configuration from Fig. 11b varies from 60° to 180° depending on the plane of observation. The phase field predictions thus account for the different stacking behavior observed experimentally between different hydride variants. (For interpretation of the references to colour in this figure legend, the reader is referred to the web version of this article.)

tensor. Furthermore, unlike other recent phase field hydride models, no shear strain was introduced in the elastic description of the current model [52,53]. Although this shear strain was shown to be crucial to predict hydride morphology in those studies, the phase transformation mechanism proposed by Zhang et al. and described above contradicts the presence of such a large shear strain [57].

Using the assumed δ-$ZrH_{1.66}$ stiffness tensor, the model predicts that a single hydride particle growing in a single grain tends to grow along the basal plane and its shape exhibits three-fold symmetry between the α-Zr HCP structure and the δ-$ZrH_{1.66}$ FCC structure. However, disturbances such as an applied stress or the presence of other hydrides can break this symmetry, in which case hydrides tend to misorient themselves with respect to the basal plane of the matrix. In a real material, defects, residual stresses, and other imperfections are expected to break this symmetry as well. As a result, the hydride shapes shown in Fig. 7a, 7d are expected to be significantly more common than those shown in Fig. 5. Nanoscale hydride shape and orientation are thus attributed to the anisotropy of the elastic properties and eigenstrains of the α-Zr/δ-$ZrH_{1.66}$ system and its interaction with outside stresses.

The phase field model predicts different stacking behaviors depending on the hydride configuration (positions and variants). The predicted morphologies have been successfully compared with high-magnification images of hydride particles. The large disparity in experimental observations can thus be explained by the current phase field model, which supports our hypothesis. However, we were only able to compare slices of the 3D simulations of the phase field model with the 2D experimental observations. 3D TEM tomography of nanoscale zirconium hydrides would provide invaluable insights on the three-dimensional hydride particle shape and could be compared more directly with phase field model predictions.

Moreover, comparing the total free energy of the different predicted morphologies provides insights into the relative stability of the different stacking behaviors. The simulations of hydride interaction have shown that while nanoscale hydrides are prone to stacking along the basal plane to optimize elastic interaction, stack-

ing along the $[0001]_\alpha \| [111]_\delta$ direction is not favorable, even under significant applied stress. Zirconium cladding materials are heavily textured [2,112], so basal planes tend to align with the cladding circumferential direction. The current phase field model thus accounts for the experimentally observed circumferential stacking of nanoscale hydrides, at least within a single zirconium grain. However, despite showing an effect of applied stress on nanoscale hydride shape, the current model offers no mechanism for radial stacking of nanoscale hydrides since these configurations were found to be unstable. As such, the current study challenges some of the mechanisms for hydride reorientation considered in previous studies [50–53,56], which require either an extremely large applied stress of around 2 GPa or a shear strain of 19% between the two phases to take place.

The model currently neglects some physical phenomena that are known to occur in zirconium cladding and that may impact the ability of our model to predict accurate hydride behavior, including hydride reorientation. One of these phenomena is plastic deformation. Dislocations have been observed around hydrides to accommodate the large elastic deformation [10,11]. Moreover, the stress field predicted by the current phase field model is higher than the yield strength of zirconium. Introducing plastic deformation in the model would reduce the elastic energy in some areas, which would affect the stress field around the hydride and influence hydride shape and hydride interaction. However, since plasticity would likely decrease the impact of stress and elastic energy, it is unlikely it would make radial stacking of hydrides more favorable than circumferential stacking under applied stress. Another missing phenomenon is the anisotropy of the interfacial energy between the α-Zr and δ-$ZrH_{1.66}$ phases. Because of a lack of available data, the interface energy is assumed to be isotropic in the current model, which is unlikely. More DFT or MD simulations are required to provide accurate anisotropic values for the interfacial energy, but accurately simulating the alpha-Zr/delta-ZrH interfaces is challenging. Until lower scale results are available, quantifying the potential effect of the interfacial energy anisotropy on hydride shape would require a parametric study on the interfacial energy anisotropy, which lies beyond the scope of the current paper. Introducing anisotropic interfacial energy might affect hydride shape and orientation. For example, the complex shapes shown in Fig. 4 could be flattened, and the orientation of the hydride particle with respect to the basal plane as shown in Fig. 7 could be reduced by introducing interfacial energy anisotropy. However, the main conclusions on hydride stacking drawn in this study based on the role of elastic anisotropy are expected to remain valid, even when anisotropic interfacial energy is introduced in the model. Although the hydride shape and orientation might change slightly from what is predicted in this paper, the elongated shape of the hydrides has been observed experimentally, and the presence of a zone in compression above and under the hydride platelets, and in tension around their edge is unlikely to be significantly affected. The preferential stacking of hydrides along the basal plane, and the high energy of radial stacking would thus likely still be observed. Moreover, as shown in Fig. 12, the impact of the interfacial energy was small compared to the chemical and elastic energy, and therefore interfacial energy anisotropy is not expected to compensate for the elastic anisotropy of the system and lead to radial stacking. However, future work is still needed to quantify the effect of interfacial energy anisotropy on hydride shape and stacking behavior.

It is also important to realize that the zirconium grain structure interacts closely with hydrides. In zirconium cladding material, grain sizes range from 1 to 10 microns, which means that nanoscale hydrides stack across hundreds of grains to form mesoscale hydrides [2,112]. Moreover, several authors described the significant effects of the grain structure and texture on both the circumferential and radial hydrides. In particular, reorientation is more difficult in a material with larger grains [112], suggesting that the mechanisms for reorientation are influenced by the grain structure. Simulating hydride precipitation in a single grain corresponds to assuming infinitely large grains, which might suppress the mechanisms responsible for reorientation. Introducing the zirconium grain structure in the model might be the key to predicting hydride reorientation under applied stress, which is the subject of ongoing work.

Another limitation of the current phase field model is its inability, due to computational costs, to simulate hydride precipitation at the mesoscale. Whereas mesoscale hydrides can grow over several hundreds of microns in length, the current model can only simulate microstructures of several hundreds of nanometers in size. As such, the phase field model can only simulate the growth and interaction of a few nanoscale hydrides. It is believed, however, that because mesoscale hydrides are aggregates of nanoscale hydride particles, the mechanisms governing hydride morphology at the mesoscale should be first studied at the nanoscale [2]. While the current phase field model cannot scale up and simulate mesoscale hydride precipitation due to large computational costs, it can provide valuable insights on how nanoscale hydrides interact to form large mesoscale structures.

6. Conclusion

Despite considerable experimental and modeling efforts to understand hydride morphology, the mechanisms governing nanoscale and mesoscale hydride morphology remain mostly unknown. A quantitative phase field model has been developed to identify the mechanisms behind δ-$ZrH_{1.66}$ nanoscale hydride shape, orientation, and stacking behavior in a single α-Zr crystal. The parameters of the model are defined using experimental measurements when available, or lower scale modeling predictions. The current phase field model differs from previous modeling efforts by the details in the description of the elastic contribution to the system. The model accounts for the anisotropic volume misfit between the two phases, the anisotropic thermal expansion of the two lattices, and the anisotropic internal strain due to the presence of hydrogen atoms in solid solution in the zirconium matrix. Moreover, the values and orientation of the stiffness tensors of the two phases are implemented in the model in a way that (1) ensures that the experimentally observed orientation relationship between the two crystals is respected, and (2) accounts for the disparities in available δ-$ZrH_{1.66}$ stiffness tensor values.

The model can predict the experimentally observed stacking of nanoscale hydrides in a single zirconium grain. In particular, it explains some of the disparities between TEM observations of hydride particles by illustrating different stacking behaviors. This study shows that the anisotropy of the different elastic properties and strains of the system govern nanoscale hydride shape, orientation, and stacking behavior. The experimentally observed circumferential stacking of nanoscale hydrides into mesoscale hydrides is thus driven by the anisotropic elastic interaction between nanoscale hydrides.

However, the current model does not predict radial hydride stacking under applied stress. On the contrary, it shows that the radial stacking of nanoscale hydrides is unlikely in a single zirconium crystal, even under external applied loads up to 250 MPa. Future work will focus on expanding the current phase field model to account for hydride reorientation. Inspired by experimental observations showing that hydride reorientation is easier in materials with smaller grains, one of the main focuses will be to incorporate the role of the polycrystalline structure of zirconium materials on hydride morphology and reorientation.

Data Availability

The MOOSE source code can be obtained from http://mooseframework.org/.

An example of the MOOSE phase field model input files used to run the simulations is available for download in the 'Research Data' Section.

Declaration of Competing Interest

The authors declare that they have no known competing financial interests or personal relationships that could have appeared to influence the work reported in this paper.

CRediT authorship contribution statement

P.-C.A. Simon: Conceptualization, Methodology, Validation, Visualization, Writing – original draft, Writing – review & editing. **Larry K. Aagesen:** Methodology, Supervision, Conceptualization, Writing – review & editing, Funding acquisition. **Andrea M. Jokisaari:** Methodology, Supervision, Conceptualization, Writing – review & editing. **Long-Qing Chen:** Supervision, Conceptualization, Writing – review & editing. **Mark R. Daymond:** Supervision, Conceptualization, Writing – review & editing. **Arthur T. Motta:** Supervision, Conceptualization, Writing – review & editing, Funding acquisition. **Michael R. Tonks:** Methodology, Supervision, Conceptualization, Writing – review & editing.

Acknowledgements

Authors would like to thank Evrard Lacroix for his help in getting experimental images of the hydrides during his time at Penn State and for the fruitful discussions. Authors would also like to thank Fande Kong from Idaho National Laboratory for his assistance in conducting the large MOOSE simulations needed for this study.

This work was performed with the support of the DOE NEUP IRP-17-13708 project "Development of a Mechanistic Hydride Behavior Model for Spent Fuel Cladding Storage and Transportation".

This research made use of the resources of the High Performance Computing Center at Idaho National Laboratory, which is supported by the Office of Nuclear Energy of the U.S. Department of Energy and the Nuclear Science User Facilities under Contract No. DE-AC07-05ID14517. We gratefully acknowledge the support of INL Laboratory Directed Research and Development Program under project # 16-013: "Micromechanistic approach and critical experiments for quantitative predictions of delayed hydride cracking in zirconium alloys." This work was authored by Battelle Energy Alliance, LLC under Contract No. DE-AC07-05ID14517 with the U.S. Department of Energy.

Appendix A. CALPHAD free energies

The CALPHAD free energies of the α-Zr/δ-ZrH system were first developed by Dupin and then used by Jokisaari [48,74]. The molar mixing free energies are derived using $G_{mix} = G_{ref} + G_{ideal} + G_{excess}$ where G_{ref} is the reference free energy of mixing of the different phases, G_{ideal} is the free energy of mixing for an ideal solution, and G_{excess} is the excess free energy of mixing due to the deviation from the ideal mixing. The expressions of the free energies of the α and δ phases are

$$G^{o}_{\alpha,mix}(x_\alpha, T) = \Big[(1-2x_\alpha)\big(G^{o,hcp}_{Zr}(T) - H^{o,SER}_{Zr}\big) + x_\alpha\Big(G^{o,hcp}_{ZrH}(T) - H^{o,SER}_{Zr} - \frac{1}{2}H^{o,SER}_{H_2}\Big)\Big] + RT\Big[x_\alpha ln\Big(\frac{x_\alpha}{1-x_\alpha}\Big) + (1-2x_\alpha)ln\Big(\frac{1-2x_\alpha}{1-x_\alpha}\Big)\Big], \quad (A.1)$$

and

$$G^{o}_{\delta,mix}(x_\delta, T) = \frac{1}{2}\Big[(2-3x_\delta)\big(G^{o,fcc}_{Zr}(T) - H^{o,SER}_{Zr}\big) + x_\delta\big(G^{o,fcc}_{ZrH_2}(T) - H^{o,SER}_{Zr} - H^{o,SER}_{H_2}\big)\Big] + RT\Big[x_\delta ln\Big(\frac{x_\delta}{2(1-x_\delta)}\Big) + (2-3x_\delta)ln\Big(\frac{2-3x_\delta}{2(1-x_\delta)}\Big)\Big] + \frac{3x_\delta^2 - 2x_\delta}{4(x_\delta-1)^2}\Big[(x_\delta-1)L^{0,fcc}(T) + (1-2x_\delta)L^{1,fcc}(T)\Big], \quad (A.2)$$

with $G^{o,hcp}_{Zr}(T) - H^{o,SER}_{Zr}$, $G^{o,fcc}_{Zr}(T) - H^{o,SER}_{Zr}$, $G^{o,gas}_{H_2}(T) - H^{o,SER}_{H_2}$, $G^{o,hcp}_{ZrH}(T) - H^{o,SER}_{Zr} - \frac{1}{2}H^{o,SER}_{H_2}$, $G^{o,fcc}_{ZrH_2}(T) - H^{o,SER}_{Zr} - H^{o,SER}_{H_2}$, $L^{0,fcc}(T)$, and $L^{1,fcc}(T)$ derived from thermodynamic databases, as described below

$$G^{o,hcp}_{Zr}(T) - H^{o,SER}_{Zr} = -7827.595 + 125.64905T - 24.1618T\ln(T) - 4.37791\text{x}10^{-3}T^2 + 34971T^{-1}\ \text{J/mol}, \quad (A.3)$$

$$G^{o,fcc}_{Zr}(T) - H^{o,SER}_{Zr} = -227.595 + 124.74905T - 24.1618T\ln(T) - 4.37791\text{x}10^{-3}T^2 + 34971T^{-1}\ \text{J/mol}, \quad (A.4)$$

$$G^{o,gas}_{H_2}(T) - H^{o,SER}_{H_2} = -9522.98 + 78.5274T - 31.357T\ln(T) + 0.002759T^2 - 7.4639\times10^{-7}T^3 + 56582.3T^{-1}\ \text{J/mol}, \quad (A.5)$$

$$G^{o,hcp}_{ZrH}(T) - H^{o,SER}_{Zr} - \frac{1}{2}H^{o,SER}_{H_2} = -45965 + 41.6T + \big(G^{o,hcp}_{Zr}(T) - H^{o,SER}_{Zr}\big) + \frac{1}{2}\big(G^{o,gas}_{H_2}(T) - H^{o,SER}_{H_2}\big)\ \text{J/mol}, \quad (A.6)$$

$$G^{o,fcc}_{ZrH_2}(T) - H^{o,SER}_{Zr} - H^{o,SER}_{H_2} = -170490 + 208.2T - 9.47T\ln(T) + \big(G^{o,hcp}_{Zr}(T) - H^{o,SER}_{Zr}\big) + \big(G^{o,gas}_{H_2}(T) - H^{o,SER}_{H_2}\big)\ \text{J/mol}, \quad (A.7)$$

$$L^{0,fcc}(T) = 14385 - 6.0T\ \text{J/mol}, \quad (A.8)$$

and

$$L^{1,fcc}(T) = -106445 + 87.3T\ \text{J/mol}. \quad (A.9)$$

These molar energies can be converted in free energy densities by using the molar volume of α-Zr $V_M = 1.4\times10^{22}$ nm^3/mol.

Appendix B. Link between free energies and TSS$_D$

Using the CALPHAD free energies of the α-Zr and δ-ZrH phases reproduced in Appendix A, it is possible to derive the value of the hydrogen solubility limit (TSS$_D$). By using the common tangent method to derive the equilibrium concentration of hydrogen in the α phase at different temperatures T, we determine the TSS$_D(T)$. These values can then be fitted using an Arrhenius law to find

$$TSS_D(T) = A\exp\Big(-\frac{Q}{RT}\Big) \quad (B.1)$$

where $A = 197081$ wt.ppm is a constant, $Q = 38960$ J/mol is the activation barrier, R is the gas constant in J/K/mol, and T the temperature in Kelvin. Fig. B1 shows how the TSS$_D(T)$ derived using the CALPHAD free energies compare with experimentally measured TSS$_D(T)$ values. The value derived here falls within the scatter of the experimental measurements.

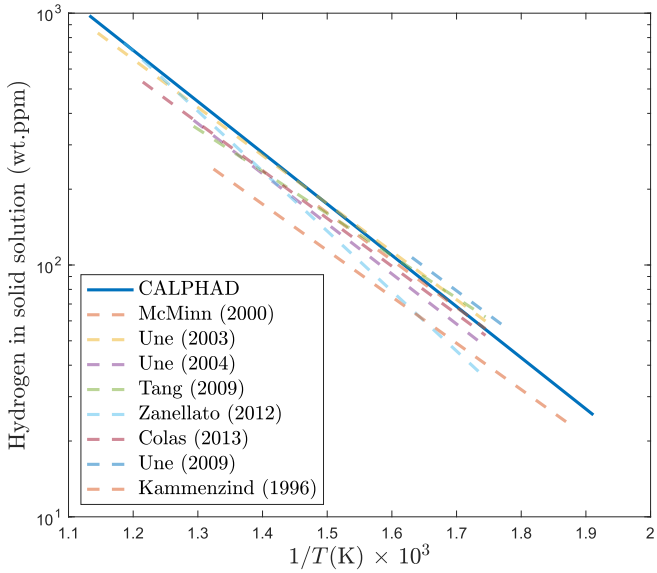

Fig. B1. Comparison of the $\mathrm{TSS}_D(T)$ derived using the CALPHAD free energies against experimental measurements [3,31,41,125–129]. The solubility limit derived theoretically falls within the scatter of the experimental measurements.

Because the parabolic approximations derived in Section 2.2.1 conserve the same equilibrium concentrations as the CALPHAD free energies, the phase field model presented in this paper predicts the TSS_D at the simulated temperature. It is important to note that deriving the supersolubility limit (TSS_P) cannot be done based on the CALPHAD free energies alone. The TSS_P is related to the hydride nucleation barrier [7,8], not the value of the thermodynamical equilibrium energies alone.

Appendix C. Derivation of the rotation angles to respect the orientation relationship between the α-Zr and δ-ZrH phases for stiffness tensors

C1. Derivation of the rotation matrix

Assuming that an orthogonal base (a_1, a_2, a_3) has to be rotated to become the base (e_1, e_2, e_3), the rotation matrix is defined as

$$Rot = \begin{pmatrix} a_1(1) & a_2(1) & a_3(1) \\ a_1(2) & a_2(2) & a_3(2) \\ a_1(3) & a_2(3) & a_3(3) \end{pmatrix} \begin{pmatrix} e_1(1) & e_2(1) & e_3(1) \\ e_1(2) & e_2(2) & e_3(2) \\ e_1(3) & e_2(3) & e_3(3) \end{pmatrix}^{-1}. \tag{C.1}$$

C2. Derivation of the Euler angles with the z-x-z convention from MOOSE

A rotation matrix can be defined using the Euler angles. However, this definition of the rotation matrix depends on the convention. The convention used in MOOSE is the extrinsic rotation z-x-z, which leads to

$$R = \begin{pmatrix} \cos(\phi)\cos(\psi) - \cos(\theta)\sin(\phi)\sin(\psi) & \cos(\psi)\sin(\phi) + \cos(\phi)\cos(\theta)\sin(\psi) & \sin(\theta)\sin(\psi) \\ -\cos(\phi)\sin(\psi) - \cos(\theta)\cos(\psi)\sin(\phi & \cos(\phi)\cos(\theta)\cos(\psi) - \sin(\phi)\sin(\psi) & \cos(\psi)\sin(\theta) \\ \sin(\phi)\sin(\theta) & -\cos(\phi)\sin(\theta) & \cos(\theta) \end{pmatrix}. \tag{C.2}$$

where (ϕ, θ, ψ) are the Euler angle for the rotations around the axis x, z, and x, respectively. Assuming that ϕ and ψ are not equal to $\frac{\pi}{2}$ and θ is not equal to 0, the Euler angles (ϕ, θ, ψ) can thus be derived from the rotation matrix derived in Eq. (C.1) using

$$\phi = atan2(Rot_{31}, -Rot_{32}), \tag{C.3}$$

$$\theta = acos(Rot_{33}), \tag{C.4}$$

and

$$\psi = atan2(Rot_{13}, Rot_{23}). \tag{C.5}$$

For a 3D simulation, (e_1, e_2, e_3)=([100], [010], [001]), $(a_1, a_2, a_3)_\alpha$ = ($[11\bar{2}0]$, $[\bar{1}100]$, [0001]), and $(a_1, a_2, a_3)_\delta$ = ($[1\bar{1}0]$, $[11\bar{2}]$, [111]). This leads to (ϕ, θ, ψ)=(30,0,0) for the Euler angles for the rotation of the α-Zr phase, and (ϕ, θ, ψ)=(135,54.7356,180) or (ϕ, θ, ψ)=(135,54.7356,0) for the two δ-$\mathrm{ZrH}_{1.66}$ variants.

Appendix D. Derivation of the eigenstrain for the volume misfit between the α-Zr and δ-$\mathrm{ZrH}_{1.66}$ phases.

The values of the eigenstrain due to the volume misfit between the two phases can be derived from the crystallographic structures. First, it is important to use appropriate values for the lattice parameters of the two phases. The lattice parameters of pure HCP α-zirconium have been measured at different temperatures ranging from 298 K to 1143 K using X-ray diffraction [107]. The lattice parameters were found to be $a = 0.323$ nm and $c = 0.514$ nm at $T = 298$ K, which is consistent with other measurements [12,14,95]. The thermal expansion coefficients were measured to be $5.50 \times 10^{-6}\ ^\circ C^{-1}$ and $10.8 \times 10^{-6}\ ^\circ C^{-1}$ along the a and the c axis, respectively [107]. The presence of hydrogen atoms in solid solution in the hexagonal crystal structure of the α-Zr phase can increase the lattice parameter. Using neutron diffraction, MacEwen et al. have measured the dilatation of HCP α-Zr by interstitial deuterium at 727 K and 777 K [105]. The lattice strain is proportional to the hydrogen content in solid solution. The coefficient of proportionality is isotropic along the basal plane and measured at $\lambda_a = 0.033$ and $\lambda_c = 0.054$ along the a and c direction, respectively.

The lattice parameter of the FCC δ-$\mathrm{ZrH}_{1.66}$ phase has been measured by performing synchrotron X-ray diffraction experiments on powder δ-hydrides [103]. At the reference temperature $T = 293.15$ K, the lattice parameter was measured to be $a = 0.478$ nm, and the thermal expansion coefficient of pure δ-$\mathrm{ZrH}_{1.66}$ was measured to be $14.1 \times 10^{-6}\ ^\circ C^{-1}$. These measurements are consistent with other studies [12,14,101,102]. It is important to note, however, that these values differ when the hydrides are inside a zirconium matrix because hydrides are then under compression.

As shown in Fig. D1, the two crystallographic structures with lattice parameters listed above do not accommodate each other. Along the $[0001]_\alpha$ direction, the basal planes of the HCP α-Zr phase need to align with the $\{111\}_\delta$ planes, as shown in Figs. D1a and D1b. Within the basal planes, the hexagonal structure needs to accommodate the atoms on the $(111)_\delta$ plane, as shown in Fig. D1c. These conditions imply that the volume misfit between the two phases leads to the following deformations:

$$\begin{cases} [0001]_\alpha : c_\alpha \rightarrow \frac{2}{\sqrt{3}} a_\delta \\ [11\bar{2}0]_\alpha : a_\alpha \rightarrow \frac{\sqrt{2}}{2} a_\delta. \\ [\bar{1}100]_\alpha : a_\alpha \rightarrow \frac{\sqrt{2}}{2} a_\delta \end{cases} \tag{D.1}$$

In addition to these deformations, the ABABAB stacking of the hexagonal structure needs to shear into an ABCABC stacking to accommodate the FCC structure. Fig. D1c shows that the third basal plane (green) does not accommodate the atoms on the $(111)_\delta$

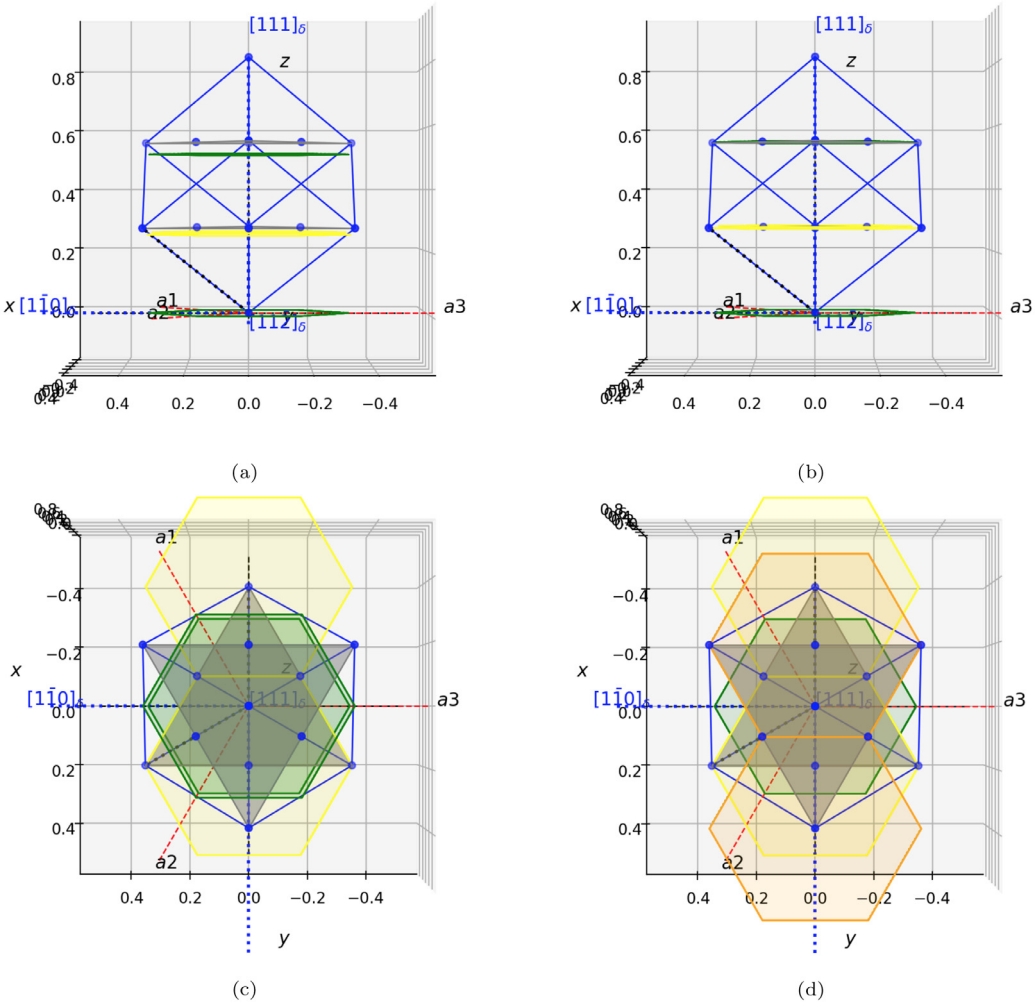

Fig. D1. Illustration of the deformation required to accommodate the FCC and HCP crystal structures. The green and yellow hexagons represent the $(0001)_\alpha$ planes of type A and B of the hexagonal α-Zr phase respectively, the blue cube represents the FCC δ-ZrH structure, and the gray triangles represent the $\{111\}_\delta$ planes. (a) shows the misfit between the two phases in $[0001]_\alpha$ direction, where the basal planes of the hexagonal structure are supposed to align with the $\{111\}_\delta$ planes. (b) shows how the crystal structure align after appropriate deformation in the $[0001]_\alpha$ direction. (c) shows how the basal plane of the HCP α-Zr phase (yellow) align with the atoms of the first $(111)_\delta$ plane after appropriate deformations. It also shows that the third basal plane does not accommodate the atoms on the second $(111)_\delta$ plane. For these to align, a shear is necessary to change the ABAB stacking of the HCP structure to the ABCABC stacking of the FCC structure, as shown in (d). These figures have been produced using a Python code developed with Jesse Carter from the Naval Nuclear Laboratory. (For interpretation of the references to colour in this figure legend, the reader is referred to the web version of this article.)

plane, until a shear in the $[10\bar{1}0]_\alpha$, $[\bar{1}100]_\alpha$, or $[0\bar{1}10]_\alpha$ direction takes place, as illustrated in Fig. D1d. Assuming that these shear deformations all happen in the same direction, authors of Refs. [52,53] argue that the phase transformation results in a large shear strain of around 19% at the scale of the hydride. However, Zhang et al. and Louchez et al. have shown that these shear deformations are more likely to happen in all three possible directions, thus resulting in no shear strain at the scale of the hydride [57,58]. Without shear strain, the lattice transformation matrix from α-Zr to δ-$ZrH_{1.66}$ is equal to

$$U = \begin{bmatrix} \frac{\sqrt{2}}{2}\frac{a_\delta}{a_\alpha} & 0 & 0 \\ 0 & \frac{\sqrt{2}}{2}\frac{a_\delta}{a_\alpha} & 0 \\ 0 & 0 & \frac{2}{\sqrt{3}}\frac{a_\delta}{c_\alpha} \end{bmatrix}. \tag{D.2}$$

Which, using a small-strain approximation, provides the eigenstrain values for the volume misfit

$$\epsilon^{*,mis}_{ij,\delta} = \frac{1}{2}(U^T + U) - I, \tag{D.3}$$

where U^T is the transpose of U and I is the identity matrix. It is reassuring to note that these $\epsilon^{*,mis}_{ij,\delta}$ coefficients at $T = 298.15$ K, provided in Table 4, sum up to 0.17. These values correspond to the coefficients and 17.2% volume change value reported by Carpenter [12].

Appendix E. Sample preparation

To validate the model and compare the simulation results with experimental observations, hydrided samples were prepared and imaged. The samples were made from Zircaloy-4 sheet material provided by ATI Specialty Alloys and Components. The native oxide of the samples was removed using an etching solution of 10% hydrofluoric acid (49% concentrated), 45% nitric acid (89% concentrated), and 45% of deionized water until the surface had a mirror finish. A 20 nm layer of nickel was then sputtered onto the etched surface of the samples to protect them against air corrosion and favor hydrogen uptake, using a Kurt J. Lesker CMS (Combinatorial Material Science) series sputter machine. Hydrogen was introduced in the samples by using the gaseous charging technique, which was described in [6].

Once hydrided, the zirconium matrix was first recrystallized at 873 K for 3 hours to obtain conditions closer to the single grain

conditions simulated in this study. After a 3h hold at 873 K, the sample was cooled down to 573 K at a rate of 15 K/min and held at that temperature for 5 hours, to allow for isothermal hydride growth to happen, as was simulated in this study. The sample was then cooled down to room temperature at 15 K/min, set in epoxy, polished and etched for 5 seconds with a cotton swab. A 4 nm layer of iridium was deposited on the surface of the sample to reduce the charging of the epoxy during SEM imaging. SEM images were acquired using an FEI Helios scanning electron microscope secondary electron detector, which allowed to capture high-resolution images of sub-micron features in the zirconium matrix such as grain boundaries, second phase particles, and nanoscale hydrides.

References

[1] D.R. Olander, A.T. Motta, Light Water Reactor materials volume I: Fundamentals, American Nuclear Society, 2017. http://www.ans.org/store/item-350026/

[2] A.T. Motta, L. Capolungo, L.Q. Chen, M.N. Cinbiz, M.R. Daymond, D.A. Koss, E. Lacroix, G. Pastore, P.C.A. Simon, M.R. Tonks, B.D. Wirth, M.A. Zikry, Hydrogen in zirconium alloys: a review, J. Nucl. Mater. 518 (2019) 440–460, doi:10.1016/j.jnucmat.2019.02.042. https://www.sciencedirect.com/science/article/pii/S0022311518316763

[3] B. Kammenzind, D. Franklin, H. Peters, W. Duffin, Hydrogen pickup and redistribution in alpha-annealed zircaloy-4, Zirconium in the Nuclear Industry: Eleventh International Symposium STP 1295 (1996) 338–370, doi:10.1520/STP16180S. http://www.astm.org/doiLink.cgi?STP16180S

[4] A. Couet, Hydrogen Pickup Mechanism of Zirconium Alloys, The Pennsylvania State University, 2014 Ph.D. thesis. http://adsabs.harvard.edu/abs/2014PhDT

[5] A. Couet, A.T. Motta, R.J. Comstock, Hydrogen pickup measurements in zirconium alloys: relation to oxidation kinetics, J. Nucl. Mater. 451 (1–3) (2014) 1–13, doi:10.1016/J.JNUCMAT.2014.03.001. https://www.sciencedirect.com/science/article/pii/S0022311514001081?via%3Dihub

[6] E. Lacroix, A.T. Motta, J.D. Almer, Experimental determination of zirconium hydride precipitation and dissolution in zirconium alloy, J. Nucl. Mater. 509 (2018) 162–167, doi:10.1016/j.jnucmat.2018.06.038. https://www.sciencedirect.com/science/article/pii/S0022311517317798

[7] E. Lacroix, Modeling Zirconium Hydride Precipitation and Dissolution in Zirconium Alloys, The Pennsylvania State University, 2019 Ph.D. thesis. http://ezaccess.libraries.psu.edu/login?url=https://www-proquest-com.ezaccess.libraries.psu.edu/docview/2432871093?accountid=13158

[8] E. Lacroix, P.-C. Simon, A. Motta, J. Almer, Zirconium hydride precipitation and dissolution kinetics in zirconium alloys, in: Zirconium in the Nuclear Industry: 19th International Symposium, ASTM STP 1597, 2021, pp. 67–91.

[9] F. Passelaigue, E. Lacroix, G. Pastore, A.T. Motta, Implementation and validation of the hydride nucleation-growth-dissolution (HNGD) model in BISON, J. Nucl. Mater. 544 (2020) 152683, doi:10.1016/j.jnucmat.2020.152683.

[10] Z. Zhao, M. Blat-Yrieix, J.-P. Morniroli, A. Legris, L. Thuinet, Y. Kihn, A. Ambard, L. Legras, M. Limback, B. Kammenzind, S.W. Dean, Characterization of zirconium hydrides and phase field approach to a mesoscopic-Scale modeling of their precipitation, J. ASTM Int. 5 (3) (2008) 101161, doi:10.1520/JAI101161. http://www.astm.org/doiLink.cgi?JAI101161

[11] J.E. Bailey, Electron microscope observations on the precipitation of zirconium hydride in zirconium, Acta Metall. 11 (4) (1963) 267–280, doi:10.1016/0001-6160(63)90182-2. http://www.sciencedirect.com/science/article/pii/0001616063901822

[12] G.J. Carpenter, The dilatational misfit of zirconium hydrides precipitated in zirconium, J. Nucl. Mater. 48 (3) (1973) 264–266, doi:10.1016/0022-3115(73)90022-6. http://www.sciencedirect.com/science/article/pii/0022311573900226

[13] C.E. Ells, Hydride precipitates in zirconium alloys (areview), J. Nucl. Mater. 28 (2) (1968) 129–151, doi:10.1016/0022-3115(68)90021-4. https://doi.org/10.1016/0022-3115(68)90021-4

[14] E. Zuzek, J.P. Abriata, A. San-Martin, F.D. Manchester, The H-Zr (hydrogen-zirconium) system, Bulletin of Alloy Phase Diagrams 11 (4) (1990) 385–395, doi:10.1007/BF02843318. http://link.springer.com/article/10.1007/BF02843318

[15] M.N. Cinbiz, D.A. Koss, A.T. Motta, J.S. Park, J.D. Almer, In situ synchrotron X-ray diffraction study of hydrides in Zircaloy-4 during thermomechanical cycling, J. Nucl. Mater. 487 (2017) 247–259, doi:10.1016/j.jnucmat.2017.02.027. http://www.sciencedirect.com/science/article/pii/S0022311516309564

[16] S. Wang, F. Giuliani, T.B. Britton, Microstructure and formation mechanisms of δ-hydrides in variable grain size Zircaloy-4 studied by electron backscatter diffraction, Acta Mater 169 (2019) 76–87, doi:10.1016/j.actamat.2019.02.042. https://arxiv.org/pdf/1811.12442.pdf

[17] H.J. Cha, J.J. Won, K.N. Jang, J.H. An, K.T. Kim, Tensile hoop stress-, hydrogen content- and cooling rate-dependent hydride reorientation behaviors of zr alloy cladding tubes, J. Nucl. Mater. 464 (2015) 53–60, doi:10.1016/j.jnucmat.2015.04.027.

[18] H.C. Chu, S.K. Wu, R.C. Kuo, Hydride reorientation in Zircaloy-4 cladding, J. Nucl. Mater. 373 (1–3) (2008) 319–327, doi:10.1016/j.jnucmat.2007.06.012. http://www.sciencedirect.com/science/article/pii/S0022311507008380?via%3Dihub

[19] S. Valance, J. Bertsch, Hydrides reorientation investigation of high burn-up PWR fuel cladding, J. Nucl. Mater. 464 (2015) 371–381, doi:10.1016/j.jnucmat.2015.05.003.

[20] P.-C.A. Simon, C. Frank, L.-Q. Chen, M.R. Daymond, M.R. Tonks, A.T. Motta, Quantifying the effect of hydride microstructure on zirconium alloys embrittlement using image analysis, J. Nucl. Mater. 547 (2021) 152817, doi:10.1016/j.jnucmat.2021.152817.

[21] L. Bell, R. Duncan, Hydride orientation in Zr-2.5% Nb; how it is affected by stress, temperature and heat treatment, Report AECL-5110 (June) (1975). https://inis.iaea.org/search/search.aspx?orig_q=RN:6217504

[22] M.C. Billone, T.A. Burtseva, R.E. Einziger, Ductile-to-brittle transition temperature for high-burnup cladding alloys exposed to simulated drying-storage conditions, J. Nucl. Mater. 433 (1–3) (2013) 431–448, doi:10.1016/j.jnucmat.2012.10.002. http://www.sciencedirect.com/science/article/pii/S0022311512005181

[23] A. Wallace, G. Shek, O. Lepik, Effects of Hydride Morphology on Zr-2.5Nb Fracture Toughness, Zirconium in the Nuclear Industry: Eighth International Symposium, ASTM International STP1023-EB, 100 Barr Harbor Drive, PO Box C700, West Conshohocken, PA 19428-2959, 2008, doi:10.1520/stp18858s. http://www.astm.org/doiLink.cgi?STP18858S

[24] H.H. Hsu, L.W. Tsay, Effect of hydride orientation on fracture toughness of Zircaloy-4 cladding, J. Nucl. Mater. 408 (1) (2011) 67–72, doi:10.1016/j.jnucmat.2010.10.068.

[25] P.A. Raynaud, D.A. Koss, A.T. Motta, Crack growth in the through-thickness direction of hydrided thin-wall Zircaloy sheet, J. Nucl. Mater. 420 (1–3) (2012) 69–82, doi:10.1016/j.jnucmat.2011.09.005. http://www.sciencedirect.com/science/article/pii/S0022311511008385

[26] J. Desquines, D. Drouan, M. Billone, M.P. Puls, P. March, S. Fourgeaud, C. Getrey, V. Elbaz, M. Philippe, Influence of temperature and hydrogen content on stress-induced radial hydride precipitation in Zircaloy-4 cladding, J. Nucl. Mater. 453 (1–3) (2014) 131–150, doi:10.1016/j.jnucmat.2014.06.049.

[27] K.N. Jang, K.T. Kim, The effect of neutron irradiation on hydride reorientation and mechanical property degradation of zirconium alloy cladding, Nuclear Engineering and Technology (2017), doi:10.1016/j.net.2017.05.006. http://www.sciencedirect.com/science/article/pii/S1738573317303327

[28] A.M. Alam, C. Hellwig, Cladding tube deformation test for stress reorientation of hydrides, in: ASTM Special Technical Publication, volume 1505 STP, American Society for Testing and Materials, 2009, pp. 635–650.

[29] D. Hardie, M.W. Shanahan, Stress reorientation of hydrides in zirconium-2.5% niobium, J. Nucl. Mater. 55 (1) (1975) 1–13, doi:10.1016/0022-3115(75)90132-4.

[30] K.B. Colas, A.T. Motta, J.D. Almer, M.R. Daymond, M. Kerr, A.D. Banchik, P. Vizcaino, J.R. Santisteban, In situ study of hydride precipitation kinetics and reorientation in Zircaloy using synchrotron radiation, Acta Mater 58 (20) (2010) 6575–6583, doi:10.1016/j.actamat.2010.07.018. http://www.sciencedirect.com/science/article/pii/S1359645410004520

[31] K.B. Colas, A.T. Motta, M.R. Daymond, J.D. Almer, Effect of thermo-mechanical cycling on zirconium hydride reorientation studied in situ with synchrotron X-ray diffraction, J. Nucl. Mater. 440 (1–3) (2013) 586–595, doi:10.1016/j.jnucmat.2013.04.047. http://www.sciencedirect.com/science/article/pii/S0022311513006557

[32] K. Colas, A. Motta, M.R. Daymond, J. Almer, Mechanisms of Hydride Reorientation in Zircaloy-4 Studied in Situ, in: Zirconium in the Nuclear Industry: 17th Volume, volume STP 1543,, 2015, pp. 1107–1137.

[33] M.N. Cinbiz, D.A. Koss, A.T. Motta, The influence of stress state on the reorientation of hydrides in a zirconium alloy, J. Nucl. Mater. 477 (2016) 157–164, doi:10.1016/j.jnucmat.2016.05.013. https://doi.org/10.1016/j.jnucmat.2016.05.013

[34] M.P. Puls, Elastic and plastic accommodation effects on metal-hydride solubility, Acta Metall. 32 (8) (1984) 1259–1269, doi:10.1016/0001-6160(84)90133-0. http://www.sciencedirect.com/science/article/pii/0001616084901330

[35] D.G. Westlake, The habit planes of zirconium hydride in zirconium and zircaloy, J. Nucl. Mater. 26 (2) (1968) 208–216, doi:10.1016/0022-3115(68)90072-X.

[36] M. Veleva, S. Arsene, M.C. Record, J.L. Bechade, J. Bai, Hydride embrittlement and irradiation effects on the hoop mechanical properties of pressurized water reactor (PWR) and boiling-water reactor (BWR) ZIRCALOY cladding tubes: part II. morphology of hydrides investigated at different magnifications and their interaction with the processes of plastic deformation, Metall. Mater. Trans. A 34 A (3) (2003) 567–578, doi:10.1007/s11661-003-0092-2. https://link.springer.com/article/10.1007/s11661-003-0092-2

[37] N. Kiran Kumar, J.A. Szpunar, Z. He, Preferential precipitation of hydrides in textured Zircaloy-4 sheets, J. Nucl. Mater. 403 (1–3) (2010) 101–107, doi:10.1016/J.JNUCMAT.2010.06.005. https://www.sciencedirect.com/science/article/pii/S0022311510002461#fig4

[38] N.A.P. Kiran Kumar, J.A. Szpunar, EBSD Studies on microstructure and crystallographic orientation of δ-hydrides in Zircaloy-4, zr-1% nb and zr-2.5% nb, Mater. Sci. Eng., A 528 (21) (2011) 6366–6374, doi:10.1016/j.msea.2011.05.022. http://www.sciencedirect.com/science/article/pii/S0921509311005594

[39] J.A. Szpunar, W. Qin, H. Li, N. Kiran Kumar, Roles of texture in controlling oxidation, hydrogen ingress and hydride formation in Zr alloys, J. Nucl. Mater. 427 (1–3) (2012) 343–349, doi:10.1016/J.JNUCMAT.2012.05.005. https://www.sciencedirect.com/science/article/pii/S002231151200236X#f0015

[40] V. Perovic, G.C. Weatherly, C.J. Simpson, Hydride precipitation in α/β zirconium alloys, Acta Metall. 31 (9) (1983) 1381–1391, doi:10.1016/0001-6160(83)90008-1. http://www.sciencedirect.com/science/article/pii/0001616083900081

[41] K. Une, K. Nogita, S. Ishimoto, K. Ogata, Crystallography of zirconium hydrides in recrystallized Zircaloy-2 fuel cladding by electron backscatter diffraction, J Nucl Sci Technol 41 (7) (2004) 731–740, doi:10.1080/18811248.2004.9715540. https://doi.org/10.1080/18811248.2004.9715540

[42] K. Une, S. Ishimoto, EBSP measurements of hydrogenated Zircaloy-2 claddings with stress-relieved and recrystallized annealing conditions, J. Nucl. Mater. 357 (1–3) (2006) 147–155, doi:10.1016/j.jnucmat.2006.06.004.

[43] D.O. Northwood, R.W. Gilbert, Hydrides in zirconium-2.5 wt. % niobium alloy pressure tubing, J. Nucl. Mater. 78 (1) (1978) 112–116, doi:10.1016/0022-3115(78)90509-3.

[44] L.-Q. Chen, Phase-Field models for microstructure evolution, Annu Rev Mater Res 32 (1) (2002) 113–140, doi:10.1146/annurev.matsci.32.112001.132041. http://www.annualreviews.org/doi/10.1146/annurev.matsci.32.112001.132041

[45] N. Moelans, B. Blanpain, P. Wollants, An introduction to phase-field modeling of microstructure evolution, Calphad: Computer Coupling of Phase Diagrams and Thermochemistry 32 (2) (2008) 268–294, doi:10.1016/j.calphad.2007.11.003. http://www.sciencedirect.com/science/article/pii/S0364591607000880

[46] I. Steinbach, Phase-field models in materials science, Modell. Simul. Mater. Sci. Eng. 17 (7) (2009) 073001, doi:10.1088/0965-0393/17/7/073001. http://stacks.iop.org/0965-0393/17/i=7/a=073001?key=crossref.20ed36695ee6f93f58944354ac62cca3

[47] H. Emmerich, Advances of and by phase-field modelling in condensed-matter physics, Adv Phys 57 (1) (2008) 1–87, doi:10.1080/00018730701822522. https://doi.org/10.1080/00018730701822522

[48] A.M. Jokisaari, K. Thornton, General method for incorporating CALPHAD free energies of mixing into phase field models: application to the α-zirconium/δ-hydride system, Calphad: Computer Coupling of Phase Diagrams and Thermochemistry 51 (2015) 334–343, doi:10.1016/j.calphad.2015.10.011. http://linkinghub.elsevier.com/retrieve/pii/S0364591615300365

[49] A.M. Jokisaari, A. M, Multiphysics phase field modeling of hydrogen diffusion and delta-hydride precipitation in alpha-zirconium, University of Michigan, 2016 Ph.D. thesis. http://adsabs.harvard.edu/abs/2016PhDT... ....33J.

[50] J. Bair, M. Asle Zaeem, D. Schwen, Formation path of δ hydrides in zirconium by multiphase field modeling, Acta Mater 123 (2017) 235–244, doi:10.1016/j.actamat.2016.10.056. http://www.sciencedirect.com/science/article/pii/S1359645416308230.

[51] J. Bair, M. Asle Zaeem, Effects of applied strain on formation, shape evolution, and reorientation of multiphase zirconium hydrides: A Multiphase field modeling study, Acta Mater (2017) Submitted. http://arxiv.org/abs/1706.01097.

[52] G. Han, Y. Zhao, C. Zhou, D.-Y. Lin, X. Zhu, J. Zhang, S. Hu, H. Song, Phase-field modeling of stacking structure formation and transition of δ-hydride precipitates in zirconium, Acta Mater 165 (2019) 528–546, doi:10.1016/J.ACTAMAT.2018.12.009. https://www.sciencedirect.com/science/article/pii/S1359645418309510#bib56.

[53] T.W. Heo, K.B. Colas, A.T. Motta, L.-Q. Chen, A phase-field model for hydride formation in polycrystalline metals: application to δ-hydride in zirconium alloys, Acta Mater (2019), doi:10.1016/J.ACTAMAT.2019.09.047. https://www.sciencedirect.com/science/article/pii/S1359645419306378.

[54] J. Bair, M. Asle Zaeem, M. Tonks, A review on hydride precipitation in zirconium alloys, J. Nucl. Mater. 466 (2015) 12–20, doi:10.1016/j.jnucmat.2015.07.014. http://www.sciencedirect.com/science/article/pii/S0022311515301008.

[55] A.T. Motta, L.Q. Chen, Hydride formation in zirconium alloys, JOM 64 (12) (2012) 1403–1408, doi:10.1007/s11837-012-0479-x. https://link.springer.com/article/10.1007/s11837-012-0479-x.

[56] B. Radhakrishnan, S. Gorti, K. Clarno, Y. Yan, Phase Field Simulations of Hydride Reorientation in Zircaloys, Technical Report, Oak RidgeNational Laboratory, Albuquerque, 2013.

[57] Y. Zhang, X.M. Bai, J. Yu, M.R. Tonks, M.J. Noordhoek, S.R. Phillpot, Homogeneous hydride formation path in α-Zr: molecular dynamics simulations with the charge-optimized many-body potential, Acta Mater 111 (2016) 357–365, doi:10.1016/j.actamat.2016.03.079. http://www.sciencedirect.com/science/article/pii/S1359645416302555.

[58] M.A. Louchez, L. Thuinet, R. Besson, A. Legris, Microscopic phase-Field modeling of hcp|fcc interfaces, Comput. Mater. Sci 132 (2017) 62–73, doi:10.1016/j.commatsci.2017.02.012. http://www.sciencedirect.com/science/article/pii/S0927025617300836.

[59] S.G. Kim, W.T. Kim, T. Suzuki, Phase-field model for binary alloys, Physical Review E 60 (6) (1999) 7186–7197, doi:10.1103/PhysRevE.60.7186. https://link.aps.org/doi/10.1103/PhysRevE.60.7186.

[60] A.A. Wheeler, W.J. Boettinger, G.B. McFadden, Phase-field model for isothermal phase transitions in binary alloys, Physical Review A 45 (10) (1992) 7424–7439, doi:10.1103/PhysRevA.45.7424. https://link.aps.org/doi/10.1103/PhysRevA.45.7424.

[61] M. Plapp, Unified derivation of phase-field models for alloy solidification from a grand-potential functional, Physical Review E - Statistical, Nonlinear, and Soft Matter Physics 84 (3) (2011) 031601, doi:10.1103/PhysRevE.84.031601. https://link.aps.org/doi/10.1103/PhysRevE.84.031601.

[62] L.K. Aagesen, Y. Gao, D. Schwen, K. Ahmed, Grand-potential-based phase-field model for multiple phases, grains, and chemical components, Physical Review E 98 (2) (2018) 023309, doi:10.1103/PhysRevE.98.023309. https://link.aps.org/doi/10.1103/PhysRevE.98.023309.

[63] A. Choudhury, B. Nestler, Grand-potential formulation for multicomponent phase transformations combined with thin-interface asymptotics of the double-obstacle potential, Physical Review E - Statistical, Nonlinear, and Soft Matter Physics 85 (2) (2012), doi:10.1103/PhysRevE.85.021602.

[64] J. Hötzer, M. Jainta, P. Steinmetz, B. Nestler, A. Dennstedt, A. Genau, M. Bauer, H. Köstler, U. Rüde, Large scale phase-field simulations of directional ternary eutectic solidification, Acta Mater 93 (2015) 194–204, doi:10.1016/j.actamat.2015.03.051.

[65] P. Steinmetz, M. Kellner, J. Hötzer, A. Dennstedt, B. Nestler, Phase-field study of the pattern formation in Al-Ag-Cu under the influence of the melt concentration, Comput. Mater. Sci 121 (2016) 6–13, doi:10.1016/j.commatsci.2016.04.025.

[66] P. Steinmetz, J. Hötzer, M. Kellner, A. Genau, B. Nestler, Study of pattern selection in 3D phase-field simulations during the directional solidification of ternary eutectic al-Ag-Cu, Comput. Mater. Sci 148 (2018) 131–140, doi:10.1016/j.commatsci.2018.02.040.

[67] M. Kellner, I. Sprenger, P. Steinmetz, J. Hötzer, B. Nestler, M. Heilmaier, Phase-field simulation of the microstructure evolution in the eutectic nial-34cr system, Comput. Mater. Sci 128 (2017) 379–387, doi:10.1016/j.commatsci.2016.11.049.

[68] Y.C. Yabansu, P. Steinmetz, J. Hötzer, S.R. Kalidindi, B. Nestler, Extraction of reduced-order process-structure linkages from phase-field simulations, Acta Mater 124 (2017) 182–194, doi:10.1016/j.actamat.2016.10.071.

[69] K. Dargahi Noubary, M. Kellner, P. Steinmetz, J. Hötzer, B. Nestler, Phase-field study on the effects of process and material parameters on the tilt angle during directional solidification of ternary eutectics, Comput. Mater. Sci 138 (2017) 403–411, doi:10.1016/j.commatsci.2017.07.006.

[70] P.C.A. Simon, L.K. Aagesen, A.T. Motta, M.R. Tonks, The effects of introducing elasticity using different interpolation schemes to the grand potential phase field model, Comput. Mater. Sci 183 (2020) 109790, doi:10.1016/j.commatsci.2020.109790. https://linkinghub.elsevier.com/retrieve/pii/S0927025620302810.

[71] N. Moelans, A quantitative and thermodynamically consistent phase-field interpolation function for multi-phase systems, Acta Mater 59 (3) (2011) 1077–1086, doi:10.1016/j.actamat.2010.10.038. http://www.sciencedirect.com/science/article/pii/S1359645410007019.

[72] J.W. Cahn, J.E. Hilliard, Free energy of a nonuniform system. I. Interfacial free energy, J Chem Phys 28 (2) (1958) 258–267, doi:10.1063/1.1744102. http://aip.scitation.org/doi/10.1063/1.1744102.

[73] J.W. Cahn, S.M. Allen, A microscopic theory for domain wall motion and its experimental verification in fe-Al alloy domain growth kinetics, Le Journal de Physique Colloques 38 (C7) (1977) C7–51–C7–54, doi:10.1051/jphyscol:1977709. http://www.edpsciences.org/10.1051/jphyscol:1977709.

[74] N. Dupin, I. Ansara, C. Servant, C. Toffolon, C. Lemaignan, J.C. Brachet, Thermodynamic database for zirconium alloys, J. Nucl. Mater. 275 (3) (1999) 287–295, doi:10.1016/S0022-3115(99)00125-7. http://www.sciencedirect.com/science/article/pii/S0022311599001257.

[75] L.Q. Chen, W. Yang, Computer simulation of the domain dynamics of a quenched system with a large number of nonconserved order parameters: the grain-growth kinetics, Physical Review B 50 (21) (1994) 15752–15756, doi:10.1103/PhysRevB.50.15752. https://journals.aps.org/prb/abstract/10.1103/PhysRevB.50.15752.

[76] N. Moelans, B. Blanpain, P. Wollants, Quantitative analysis of grain boundary properties in a generalized phase field model for grain growth in anisotropic systems, Physical Review B - Condensed Matter and Materials Physics 78 (2) (2008) 024113, doi:10.1103/PhysRevB.78.024113. https://link.aps.org/doi/10.1103/PhysRevB.78.024113.

[77] X.H. Guo, S.Q. Shi, Q.M. Zhang, X.Q. Ma, An elastoplastic phase-field model for the evolution of hydride precipitation in zirconium. part i: smooth specimen, J. Nucl. Mater. 378 (1) (2008) 110–119, doi:10.1016/j.jnucmat.2008.05.008.

[78] S.Q. Shi, Z. Xiao, A quantitative phase field model for hydride precipitation in zirconium alloys: part i. development of quantitative free energy functional, J. Nucl. Mater. 459 (2015) 323–329, doi:10.1016/j.jnucmat.2014.03.013. http://linkinghub.elsevier.com/retrieve/pii/S0022311514001226.

[79] G.Y. Huang, B.D. Wirth, First-principles study of interfacial energy between alpha-zirconium and zirconium hydride, J Appl Phys 126 (13) (2019), doi:10.1063/1.5102176.

[80] L. Thuinet, R. Besson, Ab initio study of competitive hydride formation in zirconium alloys, Intermetallics 20 (1) (2012) 24–32, doi:10.1016/j.intermet.2011.08.005. http://www.sciencedirect.com/science/article/pii/S0966979511002603.

[81] A.G. Khachaturyan, Theory of structural transformations in solids (dover books on engineering), 2008. https://books.google.com/books?hl=en&lr=&id=xyQkAwAAQBAJ&oi=fnd&pg=PP1&ots=g8zl8M5wll&sig=iPb6FIUAyZuWJiwiF-4WLETEsRI#v=onepage&q&f=false&lr=&id=xyQkAwAAQBAJ&oi=fnd&pg=PP1&ots=g8zl8M5wll&sig=iPb6FIUAyZuWJiwiF-4WLETEsRI#v=onepage&q&f=false http://www.amazon.com/exec/obidos/redirect?tag=citeulike07-20&path=ASIN/0486462803.

[82] R. Newnham, Theory of structural transformations in solids, Mater Res Bull 19 (1) (1984) 125, doi:10.1016/0025-5408(84)90018-7. http://public.eblib.com/choice/publicfullrecord.aspx?p=1920077.

[83] D.Y. Li, L.Q. Chen, Computer simulation of morphological evolution and rafting of γ' particles in ni-based superalloys under applied stresses, Scr Mater 37 (9) (1997) 1271–1277, doi:10.1016/S1359-6462(97)00276-5.

[84] K. Ammar, B. Appolaire, G. Cailletaud, S. Forest, Combining phase field approach and homogenization methods for modelling phase transformation in elastoplastic media, Revue européenne de mécanique numérique 18 (5–6) (2009) 485–523, doi:10.3166/ejcm.18.485-523. http://ejcm.revuesonline.com/article.jsp?articleId=14048.

[85] S.Y. Hu, L.Q. Chen, A phase-field model for evolving microstructures with strong elastic inhomogeneity, Acta Mater 49 (11) (2001) 1879–1890, doi:10.1016/S1359-6454(01)00118-5.

[86] P. Yu, S.Y. Hu, L.Q. Chen, Q. Du, An iterative-perturbation scheme for treating inhomogeneous elasticity in phase-field models, J Comput Phys 208 (1) (2005) 34–50, doi:10.1016/j.jcp.2005.02.015.

[87] A. Durga, P. Wollants, N. Moelans, Evaluation of interfacial excess contributions in different phase-field models for elastically inhomogeneous systems, Modell. Simul. Mater. Sci. Eng. 21 (5) (2013) 055018, doi:10.1088/0965-0393/21/5/055018. http://stacks.iop.org/0965-0393/21/i=5/a=055018?key=crossref.b02919b9c99c232859c364e99aa3980b.

[88] A. Durga, P. Wollants, N. Moelans, A quantitative phase-field model for two-phase elastically inhomogeneous systems, Comput. Mater. Sci 99 (2015) 81–95, doi:10.1016/j.commatsci.2014.11.057. http://www.sciencedirect.com/science/article/pii/S0927025614008374.

[89] I. Steinbach, M. Apel, Multi phase field model for solid state transformation with elastic strain, Physica D 217 (2) (2006) 153–160, doi:10.1016/j.physd.2006.04.001. http://www.sciencedirect.com/science/article/pii/S0167278906001205.

[90] L.K. Aagesen, D. Schwen, K. Ahmed, M.R. Tonks, Quantifying elastic energy effects on interfacial energy in the kim-Kim-Suzuki phase-field model with different interpolation schemes, Comput. Mater. Sci 140 (2017) 10–21, doi:10.1016/j.commatsci.2017.08.005. https://www.sciencedirect.com/science/article/pii/S0927025617304111.

[91] D. Schneider, E. Schoof, O. Tschukin, A. Reiter, C. Herrmann, F. Schwab, M. Selzer, B. Nestler, Small strain multiphase-field model accounting for configurational forces and mechanical jump conditions, Computational Mechanics 2017 61:3 61 (3) (2017) 277–295, doi:10.1007/S00466-017-1458-4. https://link.springer.com/article/10.1007/s00466-017-1458-4.

[92] W. Szewc, L. Pizzagalli, S. Brochard, E. Clouet, Onset of plasticity in zirconium in relation with hydrides precipitation, Acta Mater 114 (Supplement C) (2016) 126–135, doi:10.1016/j.actamat.2016.05.025. http://www.sciencedirect.com/science/article/pii/S1359645416303639.

[93] F. Long, D. Kerr, G. Domizzi, Q. Wang, M.R. Daymond, Microstructure characterization of a hydride blister in Zircaloy-4 by EBSD and TEM, Acta Mater 129 (2017) 450–461, doi:10.1016/j.actamat.2017.03.016. http://www.sciencedirect.com/science/article/pii/S1359645417302033.

[94] H. Tummala, L. Capolungo, C.N. Tomé, Quantifying the stress state in the vicinity of a δ-hydride in α-zirconium, J. Nucl. Mater. 511 (2018) 406–416, doi:10.1016/j.jnucmat.2018.08.050. https://www.sciencedirect.com/science/article/pii/S0022311518306275.

[95] E.S. Fisher, C.J. Renken, Single-crystal elastic moduli and the hcp - bcc transformation in Ti, Zr, and Hf, Physical Review 135 (2A) (1964) A482–A494, doi:10.1103/PhysRev.135.A482. https://link.aps.org/doi/10.1103/PhysRev.135.A482.

[96] P.A. Olsson, A.R. Massih, J. Blomqvist, A.M. Alvarez Holston, C. Bjerkén, Ab initio thermodynamics of zirconium hydrides and deuterides, Comput. Mater. Sci 86 (2014) 211–222, doi:10.1016/j.commatsci.2014.01.043. http://www.sciencedirect.com/science/article/pii/S0927025614000615.

[97] W. Zhu, R. Wang, G. Shu, P. Wu, H. Xiao, First-principles study of different polymorphs of crystalline zirconium hydride, J. Phys. Chem. C 114 (50) (2010) 22361–22368, doi:10.1021/jp109185n. https://doi.org/10.1021/jp109185n.

[98] P.F. Weck, E. Kim, V. Tikare, J.A. Mitchell, Mechanical properties of zirconium alloys and zirconium hydrides predicted from density functional perturbation theory, D top Dalton Trans. 44 (43) (2015) 18769–18779, doi:10.1039/c5dt03403e.

[99] X. Zhu, D.-Y. Lin, J. Fang, X.-Y. Gao, Y.-F. Zhao, H.-F. Song, Structure and thermodynamic properties of zirconium hydrides by structure search method and first principles calculations, Comput. Mater. Sci 150 (2018) 77–85, doi:10.1016/j.commatsci.2018.03.066. http://linkinghub.elsevier.com/retrieve/pii/S0927025618302258.

[100] J. Zheng, X. Zhou, L. Mao, H. Zhang, J. Liang, L. Sheng, S. Peng, First-principles study of the relative stability of various zirconium hydrides using the special quasirandom structures approach, Int J Hydrogen Energy 40 (13) (2015) 4597–4604, doi:10.1016/j.ijhydene.2015.02.045.

[101] S. Yamanaka, K. Yoshioka, M. Uno, M. Katsura, H. Anada, T. Matsuda, S. Kobayashi, Thermal and mechanical properties of zirconium hydride, J Alloys Compd 293 (1999) 23–29, doi:10.1016/S0925-8388(99)00389-8. http://www.sciencedirect.com/science/article/pii/S0925838899003898.

[102] S. Yamanaka, K. Yamada, K. Kurosaki, M. Uno, K. Takeda, H. Anada, T. Matsuda, S. Kobayashi, Characteristics of zirconium hydride and deuteride, J Alloys Compd 330–332 (2002) 99–104, doi:10.1016/S0925-8388(01)01448-7. http://www.sciencedirect.com/science/article/pii/S0925838801014487.

[103] M.N. Cinbiz, X. Hu, K. Terrani, Thermal expansion behavior of δ-zirconium hydrides: comparison of δ hydride powder and platelets, J. Nucl. Mater. 509 (2018) 566–576, doi:10.1016/J.JNUCMAT.2018.07.026. https://www.sciencedirect.com/science/article/pii/S0022311518304021.

[104] S. Wang, S. Kalácska, X. Maeder, J. Michler, F. Giuliani, T.B. Britton, The effect of δ-hydride on the micromechanical deformation of a Zr alloy studied by in situ high angular resolution electron backscatter diffraction, Scr Mater 173 (2019) 101–105, doi:10.1016/J.SCRIPTAMAT.2019.08.006. https://www.sciencedirect.com/science/article/pii/S1359646219304762.

[105] S.R. MacEwen, C.E. Coleman, C.E. Ells, J. Faber, Dilation of h.c.p. zirconium by interstitial deuterium, Acta Metall. 33 (5) (1985) 753–757, doi:10.1016/0001-6160(85)90098-7. http://www.sciencedirect.com/science/article/pii/0001616085900987.

[106] H. Peisl, Lattice strains due to hydrogen in metals, in: Hydrogen in metals, Springer, Berlin, Heidelberg, 1978, pp. 53–74, doi:10.1007/3540087052_42. http://link.springer.com/10.1007/3540087052_42.

[107] G.B. Skinner, H.L. Johnston, Thermal expansion of zirconium between 298°k and 1600°k, J Chem Phys 21 (8) (1953) 1383–1384, doi:10.1063/1.1699227. http://aip.scitation.org/doi/10.1063/1.1699227.

[108] Y. Zhang, C. Jiang, X. Bai, Anisotropic hydrogen diffusion in α-Zr and Zircaloy predicted by accelerated kinetic monte carlo simulations, Sci Rep 7 (2017) 41033, doi:10.1038/srep41033. http://www.nature.com/articles/srep41033.

[109] J.J. Kearns, Diffusion coefficient of hydrogen in alpha zirconium, Zircaloy-2 and Zircaloy-4, J. Nucl. Mater. 43 (3) (1972) 330–338, doi:10.1016/0022-3115(72)90065-7. http://www.sciencedirect.com/science/article/pii/0022311572900657.

[110] A. Sawatzky, The diffusion and solubility of hydrogen in the alpha phase of zircaloy-2, J. Nucl. Mater. 2 (1) (1960) 62–68, doi:10.1016/0022-3115(60)90025-8. http://www.sciencedirect.com/science/article/pii/0022311560900258.

[111] C. Domain, R. Besson, A. Legris, Atomic-scale ab-initio study of the Zr-H system: I. Bulk properties, Acta Mater 50 (13) (2002) 3513–3526, doi:10.1016/S1359-6454(02)00173-8. http://www.sciencedirect.com/science/article/pii/S1359645402001738.

[112] J.J. Kearns, C.R. Woods, Effect of texture, grain size, and cold work on the precipitation of oriented hydrides in Zircaloy tubing and plate, J. Nucl. Mater. 20 (3) (1966) 241–261, doi:10.1016/0022-3115(66)90036-5. http://www.sciencedirect.com/science/article/pii/0022311566900365.

[113] M.R. Tonks, D. Gaston, P.C. Millett, D. Andrs, P. Talbot, An object-oriented finite element framework for multiphysics phase field simulations, Comput. Mater. Sci 51 (1) (2012) 20–29, doi:10.1016/j.commatsci.2011.07.028. http://www.sciencedirect.com/science/article/pii/S0927025611004204.

[114] D. Schwen, L.K. Aagesen, J.W. Peterson, M.R. Tonks, Rapid multiphase-field model development using a modular free energy based approach with automatic differentiation in MOOSE/MARMOT, Comput. Mater. Sci 132 (2017) 36–45, doi:10.1016/j.commatsci.2017.02.017. http://arxiv.org/abs/1702.06450%5Cnhttps://doi.org/10.1016/j.commatsci.2017.02.017.

[115] C.J. Permann, D.R. Gaston, D. Andrš, R.W. Carlsen, F. Kong, A.D. Lindsay, J.M. Miller, J.W. Peterson, A.E. Slaughter, R.H. Stogner, R.C. Martineau, MOOSE: Enabling massively parallel multiphysics simulation, SoftwareX 11 (2020), doi:10.1016/j.softx.2020.100430. http://arxiv.org/abs/1911.04488.

[116] D. Gaston, C. Newman, G. Hansen, D. Lebrun-Grandié, MOOSE: A parallel computational framework for coupled systems of nonlinear equations, Nucl. Eng. Des. 239 (10) (2009) 1768–1778, doi:10.1016/j.nucengdes.2009.05.021. http://www.sciencedirect.com/science/article/pii/S0029549309002635.

[117] V. Perovic, G.C. Weatherly, C.J. Simpson, The role of elastic strains in the formation of stacks of hydride precipitates in zirconium alloys, Scr. Metall. 16 (4) (1982) 409–412, doi:10.1016/0036-9748(82)90162-4. https://www.sciencedirect.com/science/article/pii/0036974882901624.

[118] H. Wang, J. Thomas, M.A. Okuniewski, V. Tomar, Constitutive modeling of δ-phase zircaloy hydride based on strain rate dependent nanoindentation and nano-scale impact dataset, Int. J. Plast. 133 (2020) 102787, doi:10.1016/j.ijplas.2020.102787.

[119] S. Suman, M.K. Khan, M. Pathak, R.N. Singh, Investigation of elevated-temperature mechanical properties of δ-hydride precipitate in Zircaloy-4 fuel cladding tubes using nanoindentation, J Alloys Compd 726 (2017) 107–113, doi:10.1016/j.jallcom.2017.07.321.

[120] K. Kese, P.A. Olsson, A.M. Alvarez Holston, E. Broitman, High temperature nanoindentation hardness and Young's modulus measurement in a neutron-irradiated fuel cladding material, J. Nucl. Mater. 487 (2017) 113–120, doi:10.1016/j.jnucmat.2017.02.014.

[121] C.H. Su, P.W. Voorhees, The dynamics of precipitate evolution in elastically stressed solids - II. particle alignment, Acta Mater 44 (5) (1996) 2001–2016, doi:10.1016/1359-6454(95)00285-5.

[122] C. Shen, J.P. Simmons, Y. Wang, Effect of elastic interaction on nucleation: i. calculation of the strain energy of nucleus formation in an elastically anisotropic crystal of arbitrary microstructure, Acta Mater 54 (20) (2006) 5617–5630, doi:10.1016/j.actamat.2006.08.012. https://www.sciencedirect.com/science/article/pii/S1359645406005623.

[123] A.M. Jokisaari, S.S. Naghavi, C. Wolverton, P.W. Voorhees, O.G. Heinonen, Predicting the morphologies of γ' precipitates in cobalt-based superalloys, Acta Mater 141 (2017) 273–284, doi:10.1016/j.actamat.2017.09.003. https://www.sciencedirect.com/science/article/pii/S1359645417307371.

[124] A.M. Jokisaari, C. Permann, K. Thornton, A nucleation algorithm for the coupled conserved-nonconserved phase field model, Comput. Mater. Sci 112 (2016) 128–138, doi:10.1016/j.commatsci.2015.10.009. http://www.sciencedirect.com/science/article/pii/S0927025615006564.

[125] A. McMinn, E. Darby, J. Schofield, The Terminal Solid Solubility of Hydrogen in Zirconium Alloys, Zirconium in the Nuclear Industry: Twelfth International Symposium, volume STP 1354, ASTM, 2000, pp. 173–195, doi:10.1520/STP14300S. http://www.astm.org/doiLink.cgi?STP14300S.

[126] K. Une, S. Ishimoto, Dissolution and precipitation behavior of hydrides in Zircaloy-2 and high fe zircaloy, J. Nucl. Mater. 322 (1) (2003) 66–72, doi:10.1016/S0022-3115(03)00320-9.
[127] R. Tang, X. Yang, Dissolution and precipitation behaviors of hydrides in N18, Zry-4 and M5 alloys, Int J Hydrogen Energy 34 (17) (2009) 7269–7274, doi:10.1016/J.IJHYDENE.2009.07.018.
[128] O. Zanellato, M. Preuss, J.Y. Buffiere, F. Ribeiro, A. Steuwer, J. Desquines, J. Andrieux, B. Krebs, Synchrotron diffraction study of dissolution and precipitation kinetics of hydrides in zircaloy-4, J. Nucl. Mater. 420 (1–3) (2012) 537–547, doi:10.1016/J.JNUCMAT.2011.11.009.
[129] K. Une, S. Ishimoto, Y. Etoh, K. Ito, K. Ogata, T. Baba, K. Kamimura, Y. Kobayashi, The terminal solid solubility of hydrogen in irradiated Zircaloy-2 and microscopic modeling of hydride behavior, J. Nucl. Mater. 389 (1) (2009) 127–136, doi:10.1016/j.jnucmat.2009.01.017. http://www.sciencedirect.com/science/article/pii/S0022311509000282.